2016

Ionic Conductivity and its Role in Oxidation Reactions

Mazin Tamimi
Lehigh University

Ionic Conductivity and its Role in Oxidation Reactions

by

Mazin Abdulla Tamimi

Presented to the Graduate and Research Committee of Lehigh University

In Candidacy for the Degree of

Doctor of Philosophy

in

Chemical Engineering

Lehigh University

September 2016

Approved and recommended for acceptance as a dissertation in partial fulfillment of the requirements for the degree of Doctor of Philosophy.

_____
Date

_____
Dissertation Director

_____
Accepted Date

Committee Members:

_____
Prof. Steven McIntosh

_____
Prof. Kai Landskron

_____
Prof. Kelly Schultz

_____
Prof. Bryan Berger

Acknowledgements

Experimentation at POWGEN was performed as part of the User Program of the Spallation Neutron Source at Oak Ridge National Laboratory, and utilization of beamline 11-BM was carried out under the mail-in program of the Advanced Photon Source, Argonne National Laboratory. Both facilities are funded by the Office of Basic Energy Sciences of the U.S. Department of Energy. Mazin Tamimi is a sponsored student supported by the Saudi Arabian Oil Company, Saudi Aramco, and we would also like to thank Lehigh University for providing additional funding related to this research.

Table of Contents

Table of Figures

List of Symbols

X_{CH_4}	Methane conversion
$f_{CH_4,in}$	Methane in, mol/s
$f_{CH_4,out}$	Methane out, mol/s
S_{C_2}	C_2 selectivity
a,b,c	Crystal unit cell lattice dimensions, Å
δ	Chemical formula deviation from full occupancy
χ^2	Goodness of fit parameter for Rietveld refinement
R_{WP}	Weighted profile R-factor (goodness of fit parameter)
U_{iso}	Isotropic atomic displacement parameter
U_{xx}	Anisotropic atomic displacement parameters
f	Form factor of an element
b	Coherent scattering length of an element/isotope

1 Abstract

In the field of solid oxide fuel cells (SOFCs), a substantial portion of research is focused on the ability of some oxide materials to conduct oxygen anions through their structure. For electrolytes, the benefits of improving bulk transport of ions are obvious: decrease the resistive losses of the electrolyte, and device efficiency goes up and higher power densities are possible. Even for cathode materials, better bulk ion transport leads to an increase in the oxygen exchange rate at the cathode surface, and the oxygen reduction reaction at the cathode surface is the rate limiting step for SOFC operation at intermediate temperatures (500-700ºC). As operation in this regime is a key step towards lowering the manufacturing cost and increasing the lifetime of devices, much effort is spent searching for new, more conductive materials, and analyzing existing materials to discover the structure-activity relationships that influence ionic conductivity.

In the first part of this work, an overview is given of the neutron powder diffraction (NPD) techniques that are used to probe the structure of the materials in later parts. In the second part, NPD was used to analyze the structures of perovskite-type cathode materials, and show that increases in bulk conductivity led to increases in the surface oxygen exchange rate of these materials. In the final part, the methods used for SOFC cathode design were applied towards the design of oxide catalysts used for certain hydrocarbon partial oxidation reactions. The reactions studied follow the Mars van Krevelen mechanism, where oxygen atoms in the catalyst are consumed as part of the reaction and are subsequently replenished by oxygen in the gas phase. Similar to SOFC cathode operation, these processes include an oxygen reduction step, so it was hypothesized that increasing the ionic conductivity of the catalysts would

improve their performance, just as it does for SOFC cathode materials. While the results are preliminary, the combination of a reference catalyst for the oxidative coupling of methane with a support with very high oxygen conductivity demonstrated a small increase in performance at low temperatures.

2 The Neutron Diffraction Technique

2.1 Introduction

Neutron scattering is a powerful tool for materials analysis, with many different techniques employed to gain unique insights into a variety of material systems. In this review we examine the use of neutron powder diffraction (NPD) to probe materials at elevated temperature, and often under controlled gas atmospheres. This forms the definition of in-situ utilized within this review: probing materials that will operate above ambient temperatures in gas atmospheres. The primary motivation for this chapter is to demonstrate the utility of such in-situ neutron diffraction techniques and to highlight the facilities available to those working in the field. The focus of this review, and the area in which the McIntosh research group focuses, is in materials with application for high temperature solid oxide fuel cells (SOFCs), ion transport membranes (ITMs), and catalysts. Additional examples of other material systems are provided to illustrate the wide application of this technique.

The majority of materials of interest for this application are crystalline mixed metal oxides, often with the perovskite, spinel or a related structure. Many show significant oxygen non-stoichiometry which is utilized, in the case of solid oxide fuel cells and membranes, to facilitate oxygen transport via a vacancy hopping mechanism or, in the case of automotive catalysis, to provide an oxygen storage capacity[1]. The oxygen anion conductivity of these materials is a function of the concentration of oxygen vacancies and the mobility of the oxygen anions; the latter being a function of the surrounding crystal structure. For example, oxygen vacancy ordering can occur, locking the vacancies at certain crystallographic sites and often dramatically decreasing ionic conductivity.

The power of neutron diffraction lies in the interaction of neutrons with these oxygen anions. X-rays interact with the electron cloud of the atom, such that the scattering intensity is directly related to the atomic number (number of electrons) of the ion. This also results in a relatively short penetration depth into materials that decreases with atomic number. In contrast, neutrons interact with the atomic nucleus, such that there is no direct correlation between scattering intensity and atomic number, and resulting in a high penetration depth for neutrons. Neutrons can also be scattered by unpaired electrons and the magnetic structure of a material, but both of these applications are outside the scope of this review. For a review of neutron scattering itself, we refer the reader to the work of Dove[2].

The result is that while an X-ray diffraction pattern contains information primarily related to the metal atoms in a mixed metal oxide, a neutron diffraction pattern contains information on both the metal atoms and the oxygen. Rietveld refinement[3–5] of this diffraction pattern can then yield a multitude of information including the crystallographic location, occupancy, and the isotropic or anisotropic atomic displacement of the atoms. These parameters are of primary interest to those working to develop materials with high oxygen mobility and resulting ionic transport. The insights that this technique can provide will be highlighted in this review.

While room temperature neutron diffraction, perhaps using quenched samples, can provide useful information on the structure of these materials, in-situ studies are required to understand what occurs under real operating conditions and to, for example, map phenomena such as phase stability in temperature-pO_2-time space. The advantage of measuring all of these parameters in a single experiment should not be understated. For example, if we wish to determine the oxygen non-stoichiometry of a material without neutron diffraction we typically turn to thermogravimetric analysis (TGA), and map the change in weight of a sample as a

function of temperature and pO_2. Aside from concerns related to accuracy and stability of the balance, this technique is only a relative measurement, requiring determination of the oxygen content in a reference sample to provide absolute oxygen stoichiometry. Furthermore, if phase transition occurs it may go unnoticed. Separate in-situ XRD experiments would be required to quantify this but would still be missing information on the distribution of oxygen across different crystallographic sites and their atomic displacement. These factors combine to create significant deviations in reported oxygen stoichiometry values for the same materials[6]. In-situ neutron diffraction solves this problem by providing simultaneous and direct measurement of the oxygen stoichiometry and crystal structure.

While the advantages of this technique are great, there are some disadvantages. Of course a neutron system is housed at a national facility requiring an application for beam time and careful planning of experiments. However, a number of facilities, including both the POWGEN instrument at the Spallation Neutron Source (SNS), Oak Ridge National Laboratory, Oak Ridge, TN, USA and the D20 diffractometer at the Institut Laue-Langevin (ILL) in Grenoble, France, are now equipped to routinely probe materials under the in-situ conditions described here. The system at the SNS was developed as a collaboration between the POWGEN instrument team and the McIntosh group specifically for this application; it is capable of temperatures up to 850ºC and in gas atmospheres to control pO_2 in the range $10^{-24} < pO_2 < 1$ atm using gases from pure H_2 to pure O_2. Thus this 'activation barrier' is perhaps more perceived than real.

The large penetration depth of neutrons implies that, compared to X-rays, neutrons are only weakly scattered resulting in comparatively long measurement times, depending on the scattering power of the sample, incoming neutron flux density, instrument configuration, and desired statistics in the data. When combined with limited beam time allocations, it can be

difficult to measure true equilibrium structures or obtain very accurate information on rapid phase transitions. Again, careful experimental planning is required.

Finally, some elements exhibit significant neutron adsorption or low scattering intensity. For example, vanadium scatters only weakly making it useful for construction of sample containers but limiting the ability to study vanadium materials of interest. Gadolinium exhibits significant neutron adsorption, removing the ability to easily study Gadolinium compounds. Other elements exhibit similar scattering making it difficult to differentiate between them and to determine their distribution across crystallographic sites. This last limitation can often be overcome by combining neutron and X-ray measurements but it does remove the advantage of an 'all in one' experiment.

In this review, we seek to highlight the advantages of in-situ neutron diffraction to probe the structure of mixed metal oxides at high temperature and, frequently, under controlled gas atmospheres. While this review is quite comprehensive, it is not an exhaustive list of all relevant studies. The reader is directed to review articles[7] for further details.

2.2 Single perovskites

Single perovskites of the general form $ABO_{3-\delta}$ are the most commonly researched structures for SOFC and ITM applications; indeed, a number of the other common structures are derivatives of this parent group. For these applications, the A-site is typically a lanthanide or alkaline earth element, with the B-site occupied by a transition metal. The A cation sits in a 12-coordinated cuboctahedral site, with the B cation in octahedral coordination. This structure is quite flexible in terms of element choice, and can accept high concentrations of dopants. Oxygen non-stoichiometry occurs when the total charge on the A- and B-site is below 6+, creating oxygen vacancies in the lattice. Oxygen anion transport occurs via a vacancy hopping

mechanism, leading researchers to enhance the vacancy concentration through aliovalent doping on the A-site, or by selecting elements that will be at least partially reduced under operating conditions[8]. The mixed oxidation states on the transition metal also leads to electronic conductivity in these materials. In terms of oxygen anion motion, the most obvious pathway for oxygen anion motion is a curved path around the central cation. This has been demonstrated through theory[9] and directly observed in $La_{0.6}Sr_{0.4}Co_{0.8}Fe_{0.2}O_{3-\delta}$ through utilization of the maximum entropy method[10] , Figure 2-1.

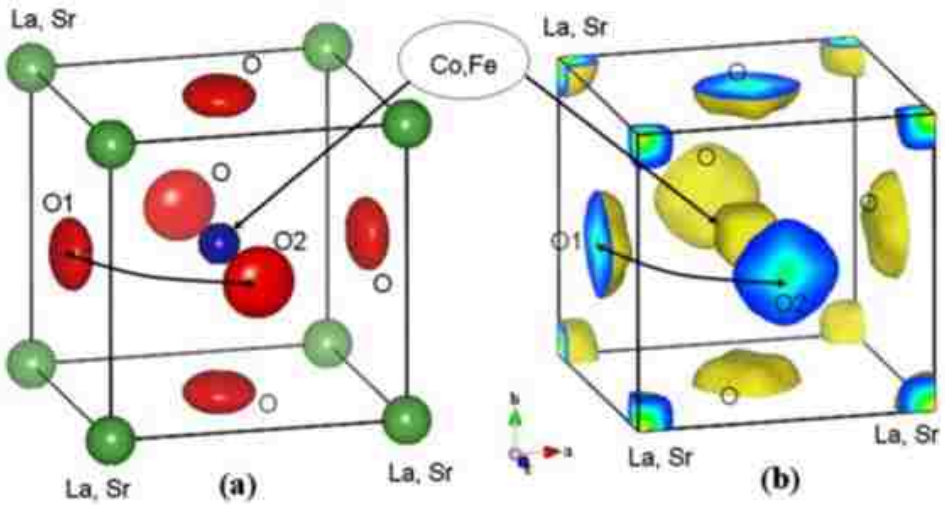

Figure 2-1 : Crystal structure (a) and nuclear density isosurface of $La_{0.6}Sr_{0.4}Co_{0.8}Fe_{0.2}O_{3-\delta}$ at 1260ºC[10]

Many studies have been performed to investigate the phase stability of the cubic perovskite and understand the structural changes under application conditions[10–12]. For example, Haag et al.[13] examined $La_{0.3}Sr_{0.7}Fe_{0.7}Cr_{0.3}O_{3-\delta}$ at 800ºC and 900ºC in atmospheres ranging in pO_2 from air to 10^{-22} atm. They showed the expected decrease in oxygen stoichiometry and associated increase in lattice parameter with decreasing pO_2. This increased lattice expansion with the formation of oxygen vacancies, termed chemical expansion, is the result of the increasing size of the B-site cation upon reduction. The material remained cubic,

space group Pm$\bar{3}$m, down to a pO_2 of 10^{-20} atm at 800ºC and 10^{-18} atm at 900ºC, at which point a spinel phase formed, followed by metallic iron below a pO_2 of $10^{-21.5}$ atm. Such material systems are of interest to application in the fuel electrode of SOFC and in ITMs for syn-gas generation.

One material that has attracted a great deal of attention is the proposed SOFC cathode and air-separation ITM material $Ba_{0.5}Sr_{0.5}Co_{0.8}Fe_{0.2}O_{3-\delta}$ that was demonstrated to provide very high performance[14]. McIntosh et al.[15] studied this material by in-situ NPD between 600 and 900ºC and between $10^{-3} < pO_2 < 1$ atm. They found that it has remarkably high oxygen non-stoichiometry with 3-δ as low as 2.192(2) at 900ºC and $pO_2 = 10^{-3}$ atm while maintaining the cubic perovskite structure, space group Pm$\bar{3}$m. This is significantly lower than may be expected to maintain this structure and is significantly lower than reported for the related material $SrCo_{0.8}Fe_{0.2}O_{3-\delta}$[16]. While potentially explaining the high oxygen ion mobility in this material, and thus its high performance, a number of groups sought to verify this finding using more traditional methods[17–21]. However, this led to numerous reports with quite differing values for oxygen stoichiometry, Figure 2-2[6]. A subsequent in-situ NPD study by Tomkiewicz et al.[6] confirmed a low oxygen stoichiometry for the related material $Ba_{0.5}Sr_{0.5}Co_{0.5}Fe_{0.5}O_{3-\delta}$. The scatter in other reported values may be due to errors in determining the oxygen stoichiometry of the reference state for their measurements, or by a phase change to a hexagonal structure during their measurements. In either case, this demonstrates the utility of NPD in simultaneously determining structure and oxygen stoichiometry.

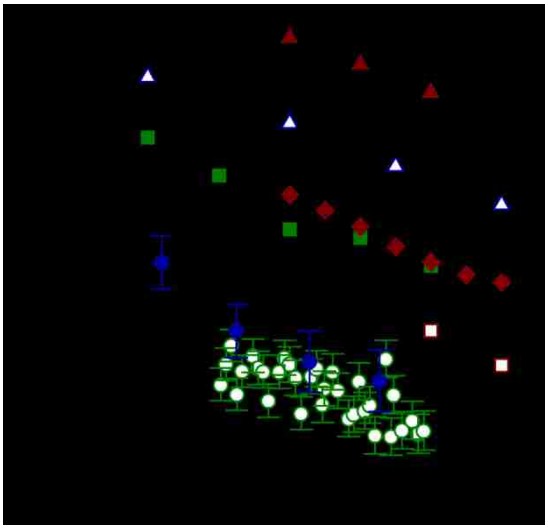

Figure 2-2 : Oxygen stoichiometry determined for $Ba_{0.5}Sr_{0.5}Co_{0.5}Fe_{0.5}O_{3-\delta}$ (closed blue circles)[6] and $Ba_{0.5}Sr_{0.5}Co_{0.8}Fe_{0.2}O_{3-\delta}$ (open green circles)[15] by in-situ NPD and for $Ba_{0.5}Sr_{0.5}Co_{0.8}Fe_{0.2}O_{3-\delta}$ by more traditional means Mueller et al.[17] (open red squares), Jung et al.[18] (closed green squares), Švarcová et al.[19] (red diamonds), Kriegel et al.[20] (open blue triangles), Bucher et al.[21] (closed red triangles).

A quite innovative study is that by Li, Maxey and Richardson[22] who examined tubular $SrFe_{0.2}Co_{0.8}O_{3-\delta}$ membranes with NPD in a specially-designed furnace that allowed for flowing different gases on either side of the membrane. Thus by exposing the sample to a pO_2 gradient, they performed not just an in-situ study but an operando study of an ITM for oxygen separation. They reported that the perovskite phase was stable down to a pO_2 of 10^{-12} atm at 900ºC without a gradient, but that it decomposes to Sr-rich n = 2,3 Ruddlesden-Popper (RP) phases, see below, and rock salt CoO below 10^{-14} atm. With an applied pO_2 gradient, they reported that the oxygen chemical potential inside the membrane was close to that at the high pO_2 side and that the chemical potential profile was quite flat across the membrane. This was derived from the observation that there was no peak broadening and that the lattice parameter was the same as the high pO_2 sample rather than an average of the high and low pO_2 samples. This indicates that oxygen removal from the membrane at the low pO_2 side is limited by surface kinetics rather than bulk transport, and that there is a sharp decrease in chemical potential at the surface

exposed to a reducing atmosphere. This high internal oxygen chemical potential stabilizes the membrane and prevents the decomposition into RP and rock salt phases, at least when the flow on the oxidizing side of the membrane is sufficient. This work demonstrates the power of in-situ NPD to provide insights into materials under realistic operating environments.

This discussion of oxygen disordered perovskites somewhat belies the complexity that can occur in these systems; a complexity that is apparent in the La1-xSrxMnOy system with x=0, 0.1, and 0.2 in Ar, 1.2%CO/Ar and dry air between RT and 950ºC[23]. Figure 2-3 shows the data for the SrMnOy sample, showing boundaries for the vacancy ordered-orthorhombic (oO $Sr_7Mn_7O_{19}$), ordered tetragonal (oT $Sr_5Mn_5O_{13}$), ordered monoclinic (oM $Sr_7Mn_7O_{19+\delta}$), vacancy disordered tetragonal (dT $Sr_5Mn_5O_{13}$), cubic (dC $SrMnO_{y-\delta}$) and stoichiometric cubic phases (sC $SrMnO_3$). The x=2 sample shows a larger region of stability for the disordered cubic phase. This thorough study contains a large quantity of data and here we discuss only one example: For x=0, the sample initially existed as a mixture of oxygen vacancy ordered orthorhombic $Sr_7Mn_7O_{19}$ and tetragonal $Sr_5Mn_5O_{13}$, but this mixture transitioned to an increasing fraction of tetragonal as it was heated and then completely to an ordered orthorhombic phase $Sr_2Mn_2O_5$. This second phase transition was complete above ~580ºC and was accompanied by a slight decomposition of the material. All of these structures have vacant sites capable of accepting non-stoichiometric oxygen, with the sites in the tetragonal and orthorhombic structures being equivalent through symmetry. Interstitial oxygen was indicated to exist in the orthorhombic $Sr_7Mn_7O_{19+\delta}$ structure. The sections below provide more examples of phase transitions that can occur, and the implications for application of these materials.

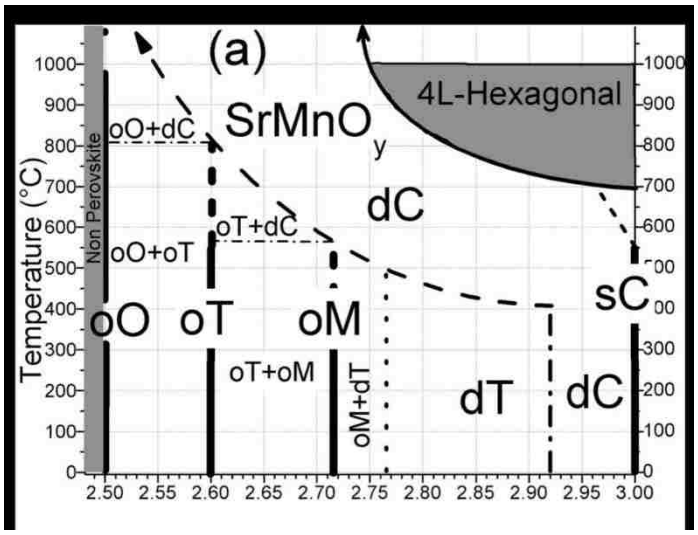

Figure 2-3 : $SrMnO_y$ phase diagram determined by Suescun et al.[23]

2.3 Double Perovskites

Double perovskites, of general form $AA'BO_{5+\delta}$, differ from single perovskite through A/A' layering along the c-axis. This leads to distortion of the cubic lattice to most commonly, at least at high temperatures, tetragonal symmetry. This layering leads to distinctly different environments for the oxygen anions. A number of reports[24–26] have now directly shown that this layering can leads to localization of oxygen vacancies within this layer. Note that this differs from the ordering observed in the Brownmillerite structure in that these vacancies are quite mobile, leading to high anisotropic oxygen anion transport rates through the a-b plane.

Cox-Galhotra and coworkers utilized in-situ NPD to examine both $PrBaCo_2O_{5+\delta}$ and $NdBaCo_2O_{5+\delta}$ finding similar results for both, from 573 to 852 ºC and $10^{-4} < pO_2 < 10^{-1}$ atm, Figure 2-4. The oxygen vacancies are localized in the Ba plane for both materials; here we provide details for the Pr material. The fractional occupancy of the O-site in the Pr layer ranges between 0.15(1) and 0.53(1), and this site shows highly anisotropic nuclear displacement in the a-b plane. The nearest neighbor O site in the Co-O plane shows a smaller number of oxygen vacancies with

fractional occupancy between 0.976(6) and 0.981(6). This site is significantly shifted towards the vacancy rich Pr layer and shows anisotropic nuclear displacement in the c-direction. The O-site in the Ba layer is, within error, fully occupied. These occupancies and the location and nuclear displacements of the sites suggests a curved oxygen transport pathway, with hopping between the vacancy rich O-site in the Pr layer and the nearest neighbor O-site in the Co layer. This pathway has been suggested by a number of studies.

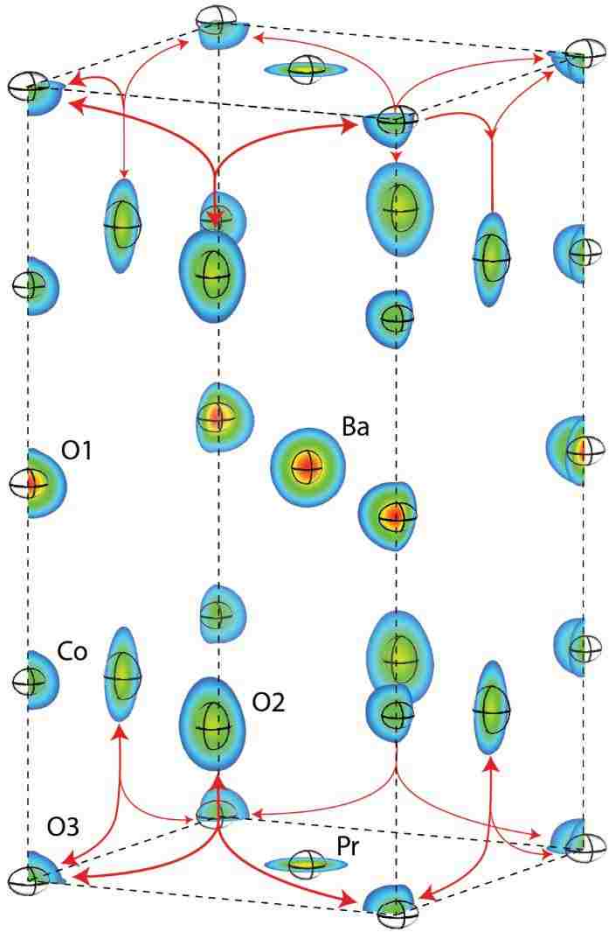

Figure 2-4 : Composite of the observed Fourier nuclear density map and thermal ellipsoids (20% probability) for $PrBaCo_2O_{5+\delta}$ (*P4/mmm*) at 10^{-1} atm oxygen and 573 °C with arrows indicating preferred oxygen transport pathways as a guide to the eye.[25]

2.4 Brownmillerite structures

The brownmillerite structure, general form $A_2B_2O_5$, is a set of alternating layers of B cations in octahedral and then in 4 tetrahedral coordination. It may be considered as a derivative of the perovskite phase with oxygen vacancies fixed in the tetrahedral coordinate layers as opposed to randomly distributed as in the cubic perovskite. The brownmillerite phase can form through vacancy ordering of the perovskite phase, and is accompanied by a dramatic decrease in oxygen anion mobility as the oxygen vacancies are 'locked' in place. McIntosh et al. examined the parent cubic perovskites $SrCo_{0.8}Fe_{0.2}O_{3-\delta}$ and observed the formation and break up of this vacancy ordered structure as a function of pO_2 and temperature. In general, as the temperature increases, the enthalpy driven formation of further oxygen vacancies in the structure overcomes the entropic ordering of oxygen vacancies required form formation of the Brownmillerite phase. Thus the Brownmillerite decomposes to a cubic perovskite as temperature increases. At pO_2=0.1 atm and temperature of 596ºC, the brownmillerite transitions to a cubic perovskite with oxygen stoichiometry refined as 2.50(2); that is, equivalent to that of the parent brownmillerite. This confirms the accuracy of neutron diffraction in determining oxygen non-stoichiometry. They found the best fit was obtained for incomplete ordering of the oxygen vacancies, space group Icmm, allowing two possible orientations of the tetrahedral, Figure 2-5. The octahedral layer showed significant distortion, with elongation of the apical Fe/Co-O bond compared to the equatorial bond. This is due to a shift in the apical oxygen towards the vacancy rich tetrahedral layer. The formation of this vacancy ordered phase, with associated shift in lattice parameter, hinders the application of this material in an ITM. Note that the phase behavior of the related material $SrFe_{0.8}Co_{0.2}O_{3-\delta}$ differs considerably as discussed above[27].

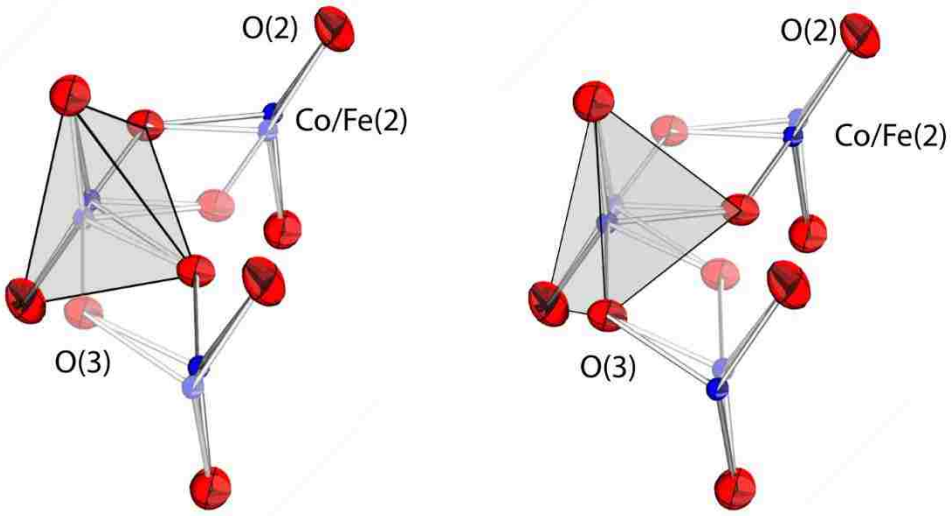

Figure 2-5 : The two possible orientations with the tetrahedral layer of the Brownmillerite phase of $Sr_2Co_{1.6}Fe_{0.4}O_5$ in the *Icmm* space group.[16]

Speakman et al.[28] studied $Ba_2In_2O_5$ via XRD and NPD in air from room temperature to 1116ºC. They concluded from the XRD and NPD data that the material had three phases: orthorhombic (either Icmm or Ibm2) from room temperature to 900ºC, tetragonal I4cm from 925ºC to 1040ºC, and cubic Pm3m above 1040ºC. The group commented that sensitivity of NPD to oxygen atoms, and the ability to measure oxygen stoichiometry in particular, is what allowed them to differentiate between related space groups. While the material is a poor oxygen conductor at intermediate temperatures, it has a sharp increase in conductivity above 925ºC. NPD pointed towards two possible phenomena that could explain anion conductivity: (1) cooperative tilting of In-O octahedral in the tetragonal phase, as indicated by larger than expected atomic displacements for the O2 and O3 atoms, and (2) a gradual transition of the O1 and O2 sites from fully ordered to fully disordered from 925-1040ºC, as indicated by a gradual decrease in O1 and O2 site stoichiometry from 1 to 5/6, and a gradual increase in O3 site stoichiometry from 0.5 to 5/6 as vacancies randomly distribute themselves among the sites.

Thus, while many Brownmillerites show low conductivity due to ordered oxygen vacancies, disordering of these vacancies creates a mobile carrier and can lead to high conductivity.

An examination of $Ba_2In_{2-x}Mo_xO_{5+3x/2}$ via XRD and NPD at room temperature, 700ºC, 750ºC, and 950ºC was conducted by Rolle et al.[29]. Due to the similar atomic numbers of molybdenum and indium (42 and 49, respectively), XRD is unable to differentiate between the elements, and NPD was essential in determining molybdenum's location in the structure. For the x=0.1 material at room temperature and 700ºC, molybdenum was entirely within the oxygen deficient layer on In2 sites. A Fourier difference map was generated from the room temperature NPD pattern of the x=0.1 material, which showed the presence of oxygen on the ¼, ¼, ¼ site, in the O3 layer. The claimed path for oxygen conduction in the tetragonal phase was hopping between O3 sites.

2.5 Ruddlesden-Popper Phases

Ruddlesden-Popper (R-P) phases have the general form $A_{n-1}A'_2B_nX_{3n+1}$ where A, A' and B are cations and X is an anion[30]; here we consider materials where X is O^{2-}. These R-P materials can be mixed oxygen anion and electronic conductors with applications in SOFC electrodes and as ITM materials. The R-P phase is commonly described as consisting of a stacking of n perovskite layers between n rock salt layers. The A cation sits in the cuboctahedral coordinated sites within the perovskites stacking layers, the A' site sits at the boundary between the rock salt and perovskites layer, and the B cation sits in the octahedral sites (assuming no anion vacancies), Figure 2-6. Thus in the n=1 structure, there are only A' sites. Neutron diffraction has great utility in, for example, identifying the position and quantity of anion vacancies, the isotropic and anisotropic displacement of the oxygen sites, and the cation distributions. These are key parameters to understanding oxygen anion transport in these materials.

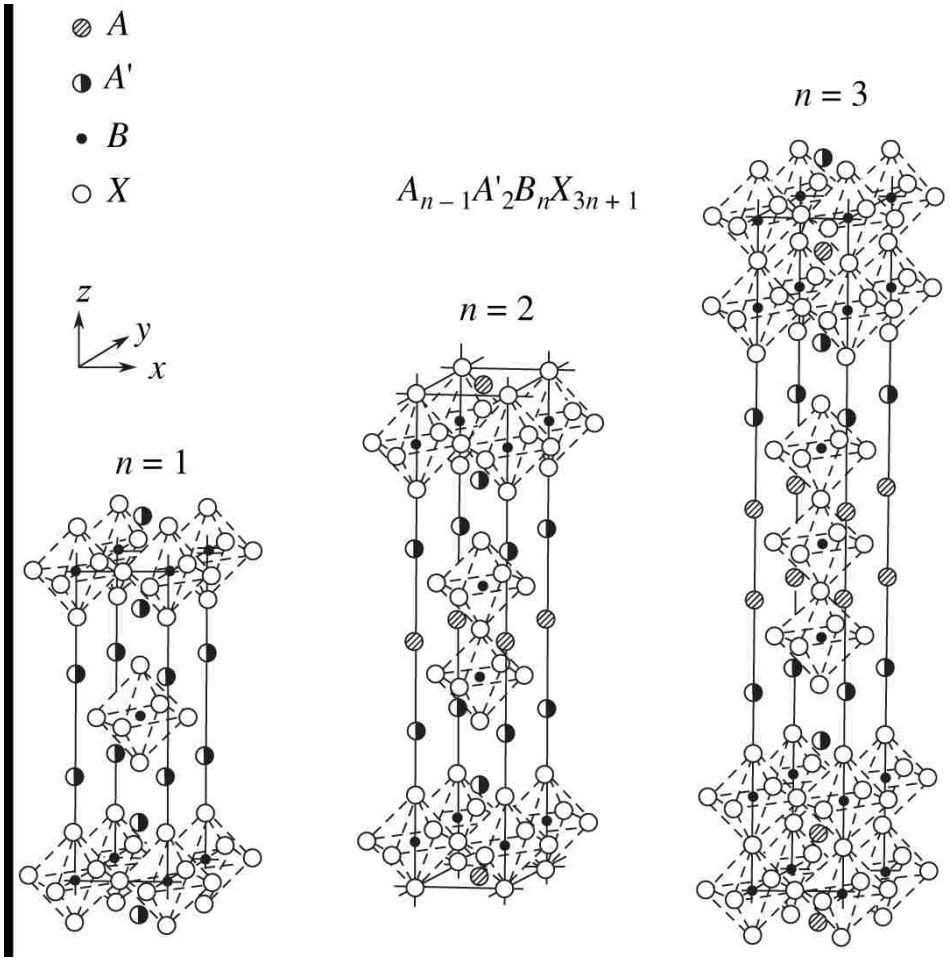

Figure 2-6 : Structure of the n=1-3 Ruddlesden-Popper phases. Adapted from [30]

Neutron diffraction experiments reveal that these materials can exhibit either oxygen hyper-stoichiometry through the incorporation of oxygen at interstitial sites, or oxygen hypo-stoichiometry through vacancy formation in the perovskite layers. Oxygen transport in these materials can occur either through an interstitial transport mechanism or via vacancy hopping. Both cases would lead to highly anisotropic oxygen transport within this a-b plane. This anisotropic transport mechanism has been confirmed through calculation[31–36] and experimentally for La_2NiO_4 by Burriel et al.[37], who measured more rapid oxygen diffusion in the a-b direction when compared with the c direction. The nature of the carrier depends on the

oxidation state of the cations, pO_2 and temperature. For example, Tonus et al.[38] observed both mechanisms in $La_{1.5+x}Sr_{0.5-x}Co_{0.5}Ni_{0.5}O_{4+\delta}$ (x = 0, 0.2) n=1 RP oxides. The samples were super-stoichiometric at room temperature with excess oxygen (δ = 0.06 and 0.12 for x = 0 and x = 0.2) located at interstitial 4d sites (0, ½, ¼) in the I4/mmm space group. Upon reduction, interstitial oxygen was the first to be removed from the structure, followed by equatorial oxygen from the perovskites layer.

Skinner[39]reported the presence of interstitial oxygen and its preferential removal during reduction for the SOFC cathode material La_2NiO_4, but similar interstitial oxygen could not be identified in the analogous $La_2Ni_{1-x}Co_xO_{4\pm\delta}$ materials[40]. Yashima et al.[41,42] generated nuclear density maps of the n=1 RP, $(Pr_{0.9}La_{0.1})_2(Ni_{0.74}Cu_{0.21}Ga_{0.05})O_{4+\delta}$, space group i4/mmm, at 606.6ºC and 1015.6ºC. These maps were generated through the maximum-entropy method (MEM), and showed a smearing of density between the apical oxygen of the perovskites layer and an oxygen interstitial site between the rock salt and perovskites layers, Figure 2-7. This was interpreted as a direct observation of oxygen atoms hopping between these sites, indicating the path for oxygen transport in this facile oxygen conductor. An increase in density along this path at the higher temperature coincides with increased oxygen transport at higher temperatures in this material.

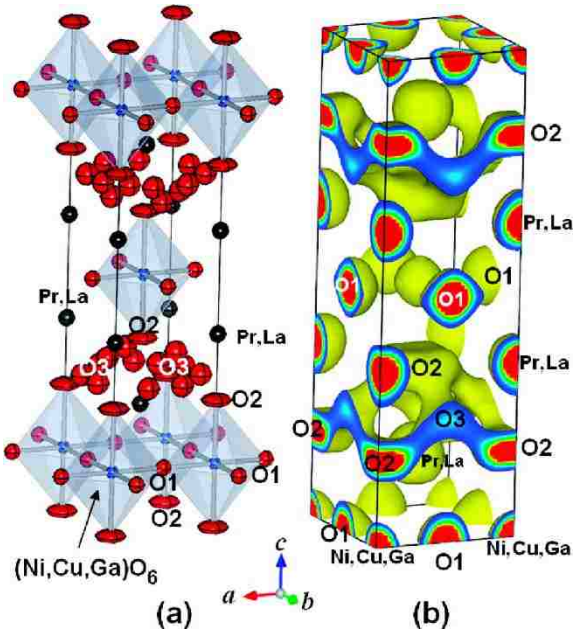

Figure 2-7 : (a) Structure and (b) isosurface of nuclear density at 0.05 fm $Å^{-3}$ of $(Pr_{0.9}La_{0.1})_2(Ni_{0.74}Cu_{0.21}Ga_{0.05})O_{4+\delta}$ at 1015.6 °C.[41]

Broux et al.[43] investigated the n=1 R-P phase $La_{1.2}Sr_{0.8}Mn_{O4+\delta}$, observing and determining the occupancy of the oxygen interstitial site. For this material, heating in oxygen induced the incorporation of a large excess of oxygen interstitials, but was accompanied by a phase transition from an initial tetragonal I4/mmm structure to an orthorhombic Bmab structure, Figure 2-8. This phase transition, complete at ~410ºC, was due to significant tilting of the octahedra in the perovskites layer due to the presence of the interstitial oxygen. Tetragonal symmetry was restored after prolonged annealing at 550ºC due to decreased octahedral tilting as the lattice thermally expanded. This final structure contained a large oxygen hyper-stoichiometry of δ≈0.42(2), ~21% occupancy of the interstitial site. It seems quite conclusive that large numbers of interstitial oxygen anions can be incorporated into these R-P phases, and that they can lead to facile oxygen transport.

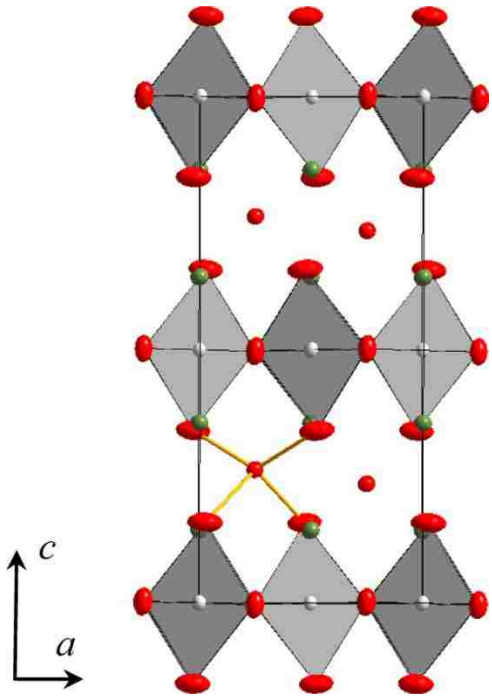

Figure 2-8 : Structural distortion around the oxygen interstitial site in the *Bmab* unit cell of $La_{1.2}Sr_{0.8}MnO_{4.30(1)}$ at 400ºC [43]

Reduction of n=1 R-P phases has been shown to lead to preferential formation of oxygen vacancies on the axial site within the perovskite layers. Bahout et al.[44] investigated the n=1 RP $Pr_{0.5}Sr_{1.5}Cr_{0.5}Mn_{0.5}O_{4-\delta}$. At room temperature, the sample had I4/mmm symmetry and was fully oxidized ($\delta = 0$). The sample was heated to 700ºC under a flow of 5% H_2-He, held at that temperature for 30 minutes, and then cooled to 60ºC. This led to expansion of the a and c axes (by 0.28% and 0.76%, respectively), and preferential removal of oxygen from the (4c) site to a fractional occupancy of 0.904, Figure 2-9, with associated increase in atomic displacement parameters. Afterwards, the sample was heated to 500ºC in air for an hour, cooled back to 60ºC, and the lattice parameters, oxygen stoichiometry and atomic displacements returned to their pre-reduced values. In situ measurements taken during the heating/cooling of the sample indicated that the crystal structure remained as I4/mmm, and no other phases or impurities

were reported. This was claimed as evidence for the high redox stability of the material, an important parameter for SOFC electrodes.

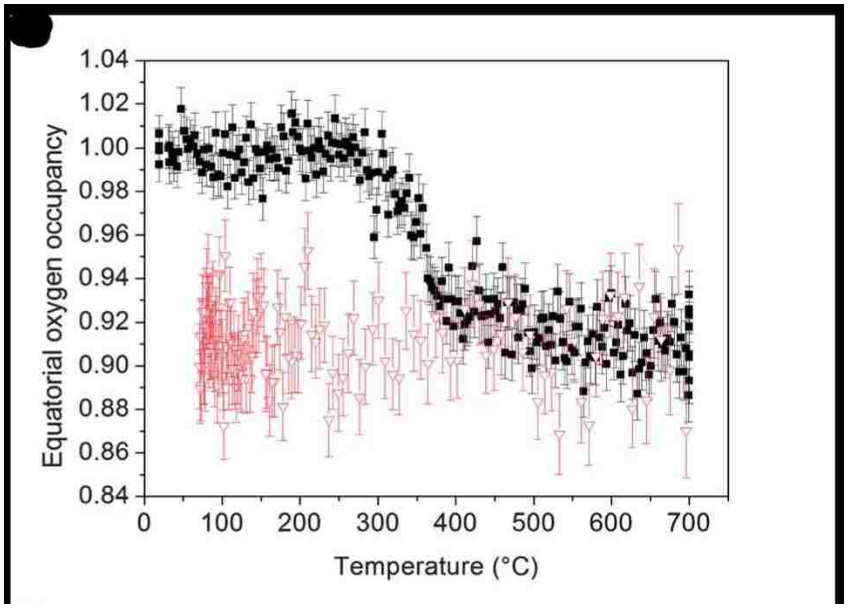

Figure 2-9 : Oxygen occupancy of the equatorial oxygen site in the n=1 Ruddlesden-Popper phase of $Pr_{0.5}Sr_{1.5}Cr_{0.5}Mn_{0.5}O_{4-\delta}$ during heating (black) and cooling (red) in 5% H_2-He[44]

Studies by Tonus et al.[45] found that $Ln_2Sr_2CrNiO_{8-\delta}$ (Ln = La, Nd), also n=1 RP oxides, followed a similar trend of reduction when heated under a flow of 5% hydrogen in helium. Again, oxygen at equatorial sites was preferentially ejected while axial oxygen sites maintained full occupancy; the majority of the oxygen loss occurred between 200-400ºC, and I4/mmm symmetry was maintained throughout heating/cooling and reduction/re-oxidation.

Maintaining the structure with disordered oxygen vacancy formation throughout the perovskites layer does not occur for all materials, and selective reduction of certain sites can lead to a phase transformation. For example, reduction of Sr_2MnO_4 leads to formation of a monoclinic phase[46] that is maintained upon cooling to room temperature in the same gas atmosphere. The oxygen vacancies are localized within the b-c plane of the monoclinic structure at room temperature, Figure 2-10, with full occupancy on the O1, O2, and O3 sites but only 11% occupancy on the O4 site.

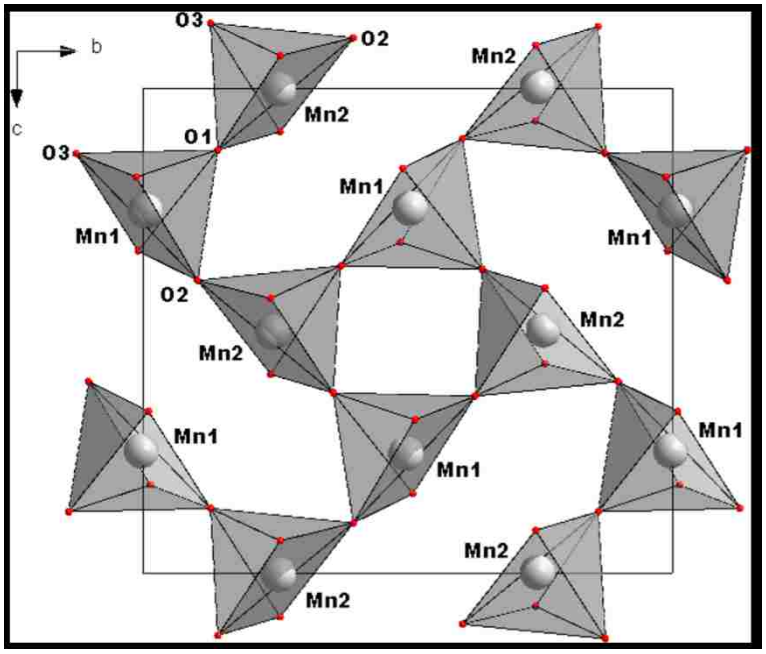

Figure 2-10 : b-c plane of the perovskite layer of the monoclinic phase of $Sr_2MnO_{3.55}$/ The O(4) site is not depicted due to the low occupancy of this site.[46]

The number of reports on n>1 R-P phases is limited. Mogni and coworkers[47] studied the n=2 Ruddlesden Popper phases of $Sr_2FeMO_{6+\delta}$ where M=Fe, Co and Ni. As may be expected by considering the relative reducibility of the cations, the total oxygen stoichiometry decreased in the order Fe>Co>Ni under the same measurement conditions. The majority of oxygen vacancies were found to be present on the O(1) site, the apical site connecting the two perovskite octahedral, with a smaller number on the O(3) site, the equatorial site of the perovskite octahedra. The apical oxygen at the boundary between the perovskite and rock salt layers was always fully occupied. This results supports the concept that oxygen transport via vacancy hopping between the sites in the perovskite layer of the structure may be generalized to higher n R-P phases. This confirmed the results of a previous report on $Sr_3Fe_2O_{6+\delta}$ by the same group[48].

2.6 Spinels – AB_2O_4

The majority of spinel compounds[49] crystallize in the Fd3m space group. The oxygen anions are arranged in a cubic close packed arrangement that yields 96 interstices in the unit cell. One eighth of the 64 tetrahedral sites and one half of the 32 octahedral sites are occupied by cations. The standard or normal configuration is that the A cation sits on the 8 tetrahedral sites, with the B cation on the 16 octahedral sites, denoted $[4]A[6]B_2O_4$. The full inverse structure sees all of the A cations move to the octahedral site and half of the B cations move to the tetrahedral site to yield $[4]B[6](AB)O_4$. Spinels can form with either extreme arrangement or with mixtures of cations across the possible range with this distribution changing as a function of temperature and pO_2. An order parameter[50], Q, is often quoted where Q=1-3/2x in $[4](A_{1-x}B_x)[6](B_{2-x}A_x)O4$. Q=1 for the normal arrangement, 0 for a random arrangement, and -0.5 for the inverse structure. Understanding the distribution of cations across sites is essential to understanding the thermal expansion behavior of these materials and their functional properties. Switching of cations between the tetrahedral and octahedral sites, or the introduction of new cations, has a significant impact on the size of the unit cell.

Redfern et al. studied the cation distribution in $MgAl_2O_4$ spinel[51], from room temperature to 1600ºC under vacuum. Since Mg^{2+} and Al^{3+} are isoelectronic, XRD cannot differentiate between them. However, the neutron scattering lengths of Mg and Al differ significantly, enabling differentiation. Redfern and coworkers directly observed an increase in the disorder across sites quantified by a decrease in Q value from ~0.8 to ~0.45 as temperature increases; that is, a shift of Mg^{2+} from tetrahedral to octahedral sites and vice-versa for Al^{3+}. This shift in relative site occupancy has a direct impact on the thermal expansion of the material and the metal oxygen bond lengths on the tetrahedral sites, Figure 2-11. As the relative occupancy

of the octahedral site by the larger Mg^{2+} atom increases above ~800K, the metal-oxygen bond lengths begins to increase much more rapidly with increasing temperature than the purely thermal expansion behavior below this transition. The tetrahedral site shows the opposite trend, showing contraction as the relative occupancy of the smaller Al^{3+} cation increases. A shift in the oxygen position is observed and directly related to this shift in bond length.

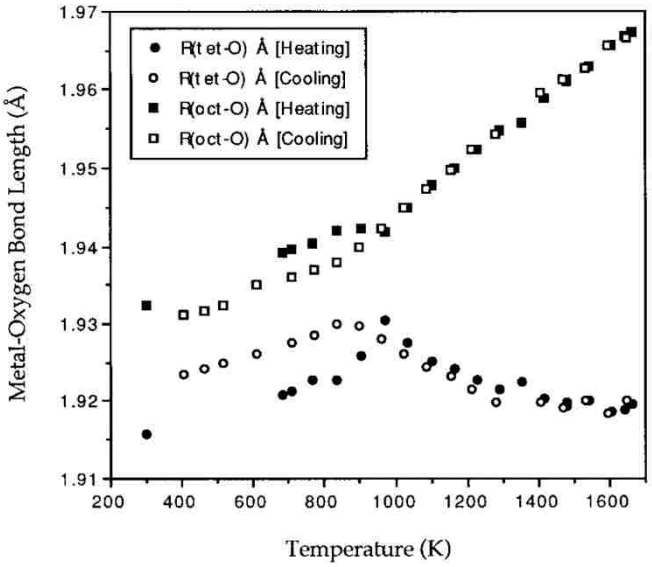

Figure 2-11 : Metal oxygen bond lengths of the tetrahedral (circles) and octahedral (squares) sites upon heating (closed) and cooling (open) Mg_2AlO_4 under vacuum[51].

This work conclusion was verified by Pavese et al.[52] who also studied cation and vacancy distributions in $MgAl_2O_4$ and also reported an increase in Al^{3+} occupancy at the tetrahedral site with increasing temperature above 944K, with concomitant decrease in the T-O bond length, again related to shift in the O-site position. As with the work of Redfern, they report a smooth variation in relative site occupancy with increasing temperature. Both groups utilized the O'Neill-Navrotsky[53] model to extract thermodynamic parameters for this order-disorder transition.

The introduction of Fe into the material to form $Mg(Fe_{0.5}Al_{0.5})_2O_4$ complicates the analysis of these materials[54]. This work combined both HTXRD and NPD techniques to enable quantification of the site distribution of all of the components. The Fe-containing material showed a similar trend to the Fe-free material; both Fe and Al shift from the tetrahedral to octahedral site, accompanied by the reverse shift for Mg, as the temperature is increased. Again, this is accompanied by a shift in the observed thermal expansion attributable to the change in cation size across sites.

A similar shift occurs in $Zn_{0.97}Fe_{2.02}O_4$ between room temperature and 1600K under vacuum[55]. As with the Mg-Al system, they observed a shift of the B-site cation from the octahedral to the tetrahedral site, an increase in disorder, with increasing temperature. Specifically, there was a shift from ~2% of the tetrahedral sites being Fe at 300K to >30% at 1500K.

In-situ powder neutron diffraction can also be utilized to map out the formation and stability of various phases. For example, Li et al.[56] examined the formation of a spinel phase through the reduction of a $CoO\text{-}2Fe_2O_3$ mixture (previously annealed at 1440ºC in air) at 900ºC under controlled oxygen partial pressures ranging from 10^{-1} to 10^{-18} atm. Figure 2-12. The partial pressure was set through a series of gas mixtures including air, Ar, CO_2, CO, 12%CO/Ar, He and O_2. The initial sample contains both a spinel phase and hematite (α-Fe_2O_3). It is suggested that this forms and the spinel fraction increases via spontaneous precipitation of Fe_3O_4 spinel at the spinel-hematite grain boundary, followed by site-mixing between the original Co-containing spinel and the new Fe-spinel. There is a smooth increase in the weight fraction of the spinel phase at the expense of the hematite phase up until $pO_2 \approx 10^{-12}$ atm, where the hematite phase fraction starts to decrease more rapidly and the spinel becomes for Fe-rich. This corresponds with a rapid increase in the lattice parameter of the spinel as the larger Fe cation occupies a

larger fraction of both octahedral and tetrahedral sites. There is then a shift lattice parameter at $pO_2 \approx 10^{-15}$ atm, a point where a Co-rich rock salt phase begins to precipitate from the bulk spinel. The increasing relative Fe content of the spinel is again accompanied by an increasing spinel lattice parameter.

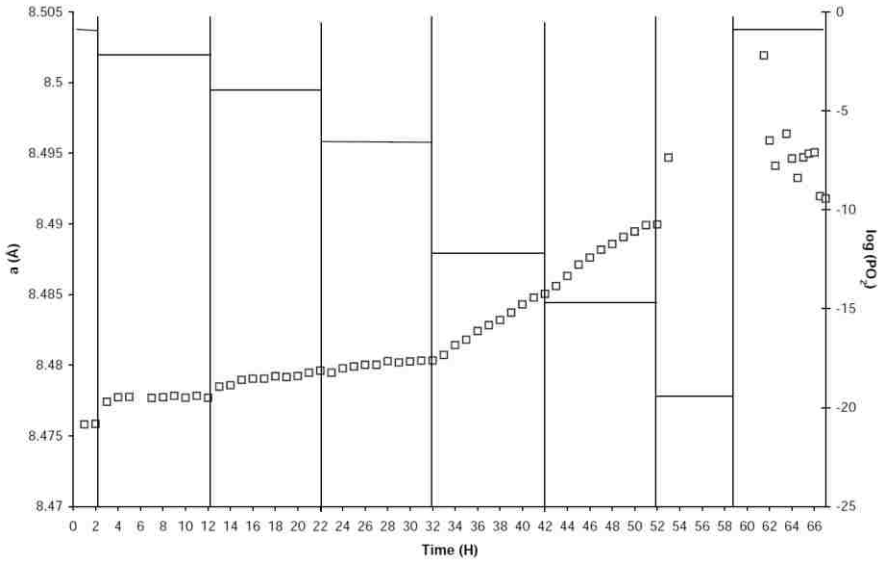

Figure 2-12 : Lattice parameter of the spinel phase formed from a $CoO\text{-}2Fe_2O_3$ mixture during reduction at 900ºC with step changes in pO_2[56].

2.7 Ceria

CeO_2 based oxides are of interest as anion conductors, catalysts, catalysts supports and as oxygen storage materials in three-way catalysts for automotive catalytic converters. This oxygen storage capacity is derived from varying the oxidation of the ceria-based oxide during pO_2 swings in the exhaust; supplying oxygen during oxygen lean operation through the creation of oxygen vacancies, and refilling these during oxygen rich operation. In all end-use cases, knowledge of the mechanism of formation, quantity, and mobility of oxygen vacancies is critical. In-situ neutron diffraction is an excellent tool to probe these materials.

In-situ studies[57] of $Ce_{0.1}Zr_{0.9}O_2$ and 0.1 wt.-% Pt/ $Ce_{0.1}Zr_{0.9}O_2$ indicated that the presence of Pt enhances the reduction of the oxide in the pO_2 range studied. This was concluded by noting that the thermal expansion of the Pt-free sample was not influenced by the presence of either oxidizing (2% O_2-Ar) or reducing (1% CO-Ar) atmospheres between RT and 700ºC. In contrast, the Pt containing sample showed an increase in the c-axis lattice parameter of the tetragonal phase of the oxide upon switching from oxidizing to reducing conditions. This was attributed to the conversion of Ce4+ to Ce3+. Unfortunately, the oxygen occupancy of the materials is not reported in this study. This concept was further underlined by a subsequent study comparing Ce-Zr solid solutions and CeO_2[58].

Li et al.[59] were able to quantify the oxygen non-stoichiometry of fluorite structured $Ce_{0.8}Y_{0.2}O_{1.9-\delta}$, an oxygen anion conducting electrolyte, as a function of equilibrium gas pO_2 at 900ºC. In addition to observing absolute oxygen stoichiometry and associated changes in the lattice parameter, Li et al. were able to correlate the isotropic atomic displacement parameter of the O-site with the non-stoichiometry, Figure 2-13, and lattice parameter. The increasing displacement with increasing non-stoichiometry and lattice parameter is suggested to reflect the mobility of the oxygen anions within the material. Note that this study hints at one limitation of neutron diffraction: the commonly utilized ion conductor $Ce_{0.8}Gd_{0.2}O_{1.9}$ is difficult to study due to the neutron adsorption of Gd.

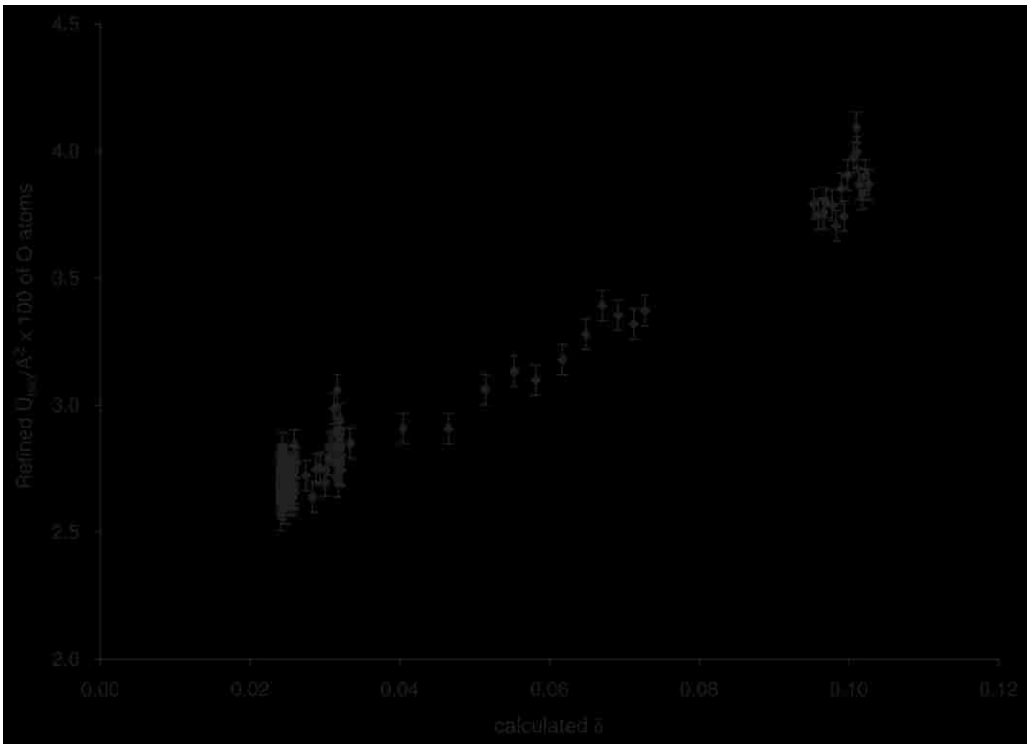

Figure 2-13 : Oxygen displacement as a function of oxygen non-stoichiometry in $Ce_{0.8}Y_{0.2}O_{1.9-\delta}$[59].

Ozawa and coworkers also studied rare earth doped ZrO_2 materials by powder neutron diffraction at room temperature[60], and performed in-situ inelastic (INS) and quasielastic neutron scattering (QENS) to examine the motion of protons in the solid oxide proton conductor, Y-doped BaCeO3[61]. This work observed a jump from primarily vibrational displacement to jump diffusion at ~500ºC. In-situ QENS had previously been used to study proton motion in the similar Yb-doped SrCeO3 system by Hempelmann et al.[62] who were able to conclude that proton transport in these materials occurs both by free diffusion and a series of trap and escape events. In free diffusion, the protons jump between oxygen ions, but they can become trapped at Yb3+ dopant ions on the Ce4+ sites in the lattice.

2.8 Some other in-situ studies of interest

There are a number of other important scientific questions that can be probed via in-situ neutron studies, from powder diffraction to the range of other techniques available. In this section we highlight a small number of these.

Other materials of interest in automotive catalysis have also been probed. Ozawa et al.[63] observed the structural changes in a Cu-Al_2O_3 NO reduction automotive exhaust catalyst as a function of temperature under vacuum. They observed complete elimination of the pure CuO phase above 800ºC due to incorporation of Cu into the underlying oxide lattice. This was accompanied by stabilization of a Cu-Al_2O_3 phase that was structurally similar to the γ-Al_2O_3 phase. In a further study of the alumina system, Loong et al.[64] examined the influence of 1 mol.-% La doping on the phase transition temperatures of Al_2O_3. They found that even such a small doping level was sufficient to shift the α-Al_2O_3formation temperature from ~1125ºC to ~1250ºC. They found that while oxygen resides on its prescribed atomic positions for all of the alumna phases, some of the Al ions shift from octahedral symmetry to tetrahedral and then back to octahedral as the phase transitions occur. It is suggested that this required diffusion of Al is hindered by the presence of the La dopant. Both studies provide invaluable insight for those seeking to understand the structure-function relationships of these catalysts.

Walton and coworkers.[65] utilized a moderate temperature in-situ cell to study the hydrothermal synthesis mechanism of $BaTiO_3$ from $Ba(OD)_{2.8}D_2O$ or $BaCl_2$ and crystalline anatase TiO_2 or amorphous $TiO_2{\cdot}H_2O$ between 125 and ~200ºC. The sample holder formed a hydrothermal bomb type reactor. Understanding the mechanism is necessary to control the growth of the powder and resulting particle size. They were able to differentiate between two competing proposed mechanisms: one involving homogenous solution phase reaction between

the reactants (dissolution-precipitation) and the other involving heterogeneous reaction between solid TiO_2 phase and soluble Ba species; confirming the dissolution-precipitation mechanism by observing dissolution of both the Ba salt and a considerable amount of TiO_2 prior to the appearance of any $BaTiO_3$. The rate of decay of TiO_2 does not mirror the rate of $BaTiO_3$ formation, suggesting that the reaction is not directly with the TiO_2 solid.

Huq et al.[66] utilized deuterium to examine hydrogenation of Li_3N, a potential hydrogen storage material, at up to 350ºC. They observed, and were able to quantify the phase fractions forming and equilibrium amounts, the reaction pathway

$$Li_3N + 2D_2 \rightarrow Li_2ND + LiD + H_2 \leftrightarrow LiND_2 + 2LiD$$

An observed increase in unit cell volume for Li_2ND upon deuteration, and corresponding decrease upon dedeuteration at 250ºC is indicative of a D non-stoichiometry in the phase to form Li_xND_{3-x}. The LiN phase shows no such change in lattice volume under the same conditions.

2.9 Summary and Outlook

In-situ powder neutron diffraction is a powerful technique for the characterization of oxides. While there are some limitations, this technique is unrivalled as a tool to probing both oxygen hypo- and hyper-stoichiometric materials. In addition to understanding phase behavior, NPD can quantify and locate oxygen interstitials and vacancies, and the isotropic and anisotropic displacement of these sites can be utilized to visualize oxygen transport pathways within the material. In this review we have sought to highlight numerous examples of how this can provide new insights into material functionality and drive future material development.

The accessibility to this technique for the research community is growing with in-situ sample environments available at both the SNS in the USA and ILL in France, and the number of

research groups routinely utilizing these facilities is growing. The next challenge is to integrate these crystallographic studies with other functional property measurements and theory to create true structure-function relationships for this class of materials, and perhaps develop a more predictive approach to new materials development.

3 Experimental Methods

3.1 LnSCF Perovskites

3.1.1 Powder Synthesis

Catalyst materials for the prior and proposed work are synthesized via a modified Pechini method[67]. Metal nitrate solutions are prepared by dissolving metal nitrate hydrates (Alfa Aesar, Ward Hill, MA) in distilled water and confirming the concentration via titration with a standard 0.1 M EDTA solution (Ricca Chemical Company, Arlington, TX). Appropriate volumes of each solution are mixed in the desired molar ratio, EDTA and citric acid are added to chelate the metal ions, and the solution is continuously mixed as it is heated to evaporate the distilled water. This leaves behind a cake of metal ions, nitrate, EDTA and citric acid, which is then combusted, so that only the metal ions remain. A final heating step overnight at elevated temperatures (800~1300ºC) can be performed to sinter the resultant oxide powder, encouraging grain growth, which enhances the sharpness of the peaks for subsequent X-ray and neutron diffraction studies.

Synthesis of the catalysts in this manner is quicker than solid state synthesis, which can require multiple 60+ hour heat cycles at the catalysts' sintering temperature, interspersed with labor-intensive grinding and pellet pressing steps. A disadvantage of this technique, however, is that the precursor metal nitrate solutions must be titrated to determine their exact concentration, as the powder form of the metal nitrates tend to be quite hygroscopic, and thus do not have stable weights once they have been exposed to air. Additionally, the titration for certain metals, such as strontium, can involve indicator changes that are difficult to detect, so

the titration must be done very carefully. But, if titrated correctly, a single batch of metal nitrate solution can be used to prepare many different catalysts, so this is usually not a grave issue.

3.1.2 Bulk Structure Determination: X-ray Diffraction & Neutron Diffraction

Neutron powder diffraction (NPD) patterns for prior work were collected at the POWGEN beamline of the Spallation Neutron Source, Oak Ridge National Laboratory, Oak Ridge, TN, USA. Experimental details are similar to those reported previously[24]. Neutrons of different wavelengths can be used to probe different d-space ranges, depending on the material, but, for the most part, 1.333 Å neutrons have been used to collect data in the *d*-space range of 0.45~4.5 Å, as this range contains most of the information of interest, and is where the instrument has the highest resolution.

Samples for *in situ* measurements were held in a 40 mm long by 10 mm diameter quartz basket with a fritted bottom. Mass flow controllers were connected to cylinders of ultra-high purity oxygen and nitrogen gases and used to control the pO_2 of the sample environments from 10^{-1} to 10^{-3} atmospheres, while keeping total pressure at one atmosphere. Outlet pO_2 was verified with a stabilized zirconia oxygen sensor (Imtech, Knoxville, TN, USA). The sample was heated by a fused silica quartz tube furnace with vanadium foil elements operating under vacuum conditions. Concentric quartz tubes were used to suspend the sample basket, separate it from the vacuum of the furnace, and provide a flow path for the gas atmosphere. Diffraction patterns were collected at temperatures in the range of 300 to 400ºC for the bismuth molybdate materials, due to the low melting point of some of the phases tested and their potential application towards acrolein production, and in the 500-800ºC range for the perovskite and perovskite-based materials, due to their potential as SOEC/SOFC cathode catalysts. In all cases, the temperature was measured by thermocouples inside the same tube as

the sample and located just above and below the neutron beam. The temperature measured via the thermocouples was converted to a sample temperature using a ZnO reference sample.

Equilibration of the sample with its environment is critical for obtaining a high quality diffraction pattern with sharp peaks, therefore diffraction patterns with short, 10-15 minute collection times were repeatedly collected and analyzed in order to confirm equilibrium after each condition change. If the main diffraction peaks for a sample were no longer shifting, it was deemed to have equilibrated. Ideally, a full Rietveld refinement modeling all parameters of interest for the material would be used, but the allotted beam time on a neutron source such as the SNS is a very limited resource, and so this quick equilibrium test was used.

Patterns for refinement were generated by collecting data until total accelerator charge had reached 3.3 coulombs, which corresponded to approximately one hour of collection time. Diffraction patterns for an empty quartz basket were recorded for each measurement temperature, and this data was subtracted from the sample scans before performing further analysis. Additional room temperature diffraction patterns were collected on the same beamline, using longer collection times and with the samples contained in sealed vanadium cans packed under a helium atmosphere. These containers do not allow for the flow of gases, making them unsuitable for *in situ* experiments that call for controlled atmospheres; however, in the case of room temperature measurements, where the kinetics of sample reduction are too slow to observe over the course of a single experiment, one can take advantage of the fact that vanadium is more transparent to neutron flux than is quartz and obtain higher quality diffraction patterns.

Synchrotron x-ray diffraction (XRD) patterns were collected at beamline 11-BM of the Advanced Photon Source, Argonne National Laboratory, Argonne, IL, USA. Sample powders were placed into 0.8 mm diameter Kapton tubes and spun at 60 Hz in a Debye–Scherrer geometry.

Measurements were performed in air at room temperature, using 0.413895 Å wavelength x-rays.

Rietveld refinements[3] of the diffraction patterns were performed with the GSAS[5] package and EXPGUI[68] interface. Refined parameters for all patterns included lattice constants and oxygen occupancy. If allowed by symmetry, oxygen positions were also refined, in general. For *in situ* NPD data, oxygen displacements were refined anisotropically if doing so significantly improved the quality of the fit, but for room temperature NPD and synchrotron XRD data, this parameter was refined isotropically. Displacement parameters for cations were always refined isotropically. Crystallite size and strain broadening was modeled with Lorentzian profile terms for the synchrotron data, and both Gaussian and Lorentzian profile terms for the neutron data.

3.1.3 Surface Structure Determination: X-ray Photoelectron Spectroscopy

For the X-ray photoelectron spectroscopy (XPS) analysis, powder samples of all three materials were pressed onto a conductive tape that was mounted onto a nickel substrate. 1486.6 eV Al Kα x-rays were used to excite the sample, and the following orbitals were used to quantify the amount of each element: 3d for La, Pr, Nd, and Sr, 2p for Co, 3p for Fe, and 1s for O and Na (an impurity discovered on the surface of the materials).

3.1.4 Cell Fabrication & Electrochemical Impedance Spectroscopy

The perovskite catalyst powders were fabricated into electrodes for electrochemical impedance spectroscopy (EIS) analysis. Powder samples of each LnSCF material were added to powders of $Gd_{0.2}Ce_{0.8}O_{1.9}$ (GDC20, Fuel Cell Materials, Columbus, OH) and graphite in a 10:10:1 mass ratio and ball milled overnight in ethanol. The resulting slurry was strained and lightly heated to remove the ethanol, then ground and mixed with glycerol to form a paste. GDC20 powder was pressed into circular pellets and fired at 1350ºC for 4 hours to form dense

electrolyte substrates with a diameter of 19 mm and a thickness of 600-800 μm. The paste was painted onto both sides of the substrate using a plain wood applicator and a stainless steel mask, and the cells were sintered at 1000ºC for 2 hours. This procedure was performed twice on each side to form symmetrical electrochemical cells with 6-8 mm diameter electrodes. Platinum ink was used as a current collector, along with platinum wire contacts, and the cells were placed in a tubular furnace in air in temperatures in the range of 400-700ºC. EIS spectra were measured using a Gamry Reference 3000™ potentiostat (Gamry Instruments, Warminster, PA) in potentiostatic mode with a perturbation of 10 mV rms. Duplicate cells were produced using a sintering temperature of 1200ºC, silver ink, and silver wire.

3.1.5 Pulsed Isotopic Oxygen Exchange

A pulse isotopic oxygen exchange technique[69,70], was performed on the perovskite and perovskite-based samples to determine their oxygen surface exchange rate. Full details of the experimental system and procedure are available elsewhere[70]. Powder samples of the materials were sieved to a 106-150 μm particle size and then loaded into quartz tubes. The packed tubes were then heated to temperatures between 575-875ºC under flowing 21% O_2/N_2 such that the sample oxygen stoichiometry equilibrated with the gas. Multiple 500 μL pulses of 97 atom% purity $^{18}O_2$ gas (Isotech, Champaign, IL) in UHP nitrogen of the same 21% $^{18}O_2/N_2$ ratio were injected into the reactor, and a residual gas analyzer (Cirrus 2, MKS Instruments UK Ltd.), was used to measure the outlet concentrations of $^{18}O_2$ and $^{16}O^{18}O$, from which surface isotopic oxygen exchange rates were calculated (the drop in $^{16}O_2$ concentration cannot be accurately measured due to the relatively long residence time in the analyzer chamber). The surface area of the samples, as measured via BET, was used to normalize the rates.

3.2 Bismuth Molybdates

$Bi_2(MoO_3)nO_3$ (n = 1,2,3) materials were synthesized via a modified Pechini method[67]. Four samples were generated, each with a distinct phase: alpha (n=3), beta (n=2), and two different polymorphs of the gamma (n=1) phase, low temperature (LT gamma) and high temperature (HT gamma). The transition from LT to HT gamma happens irreversibly at 604ºC[71], and the HT phase is metastable at room temperature. A bismuth(III) solution was prepared by dissolving bismuth nitrate pentahydrate powder (Alfa Aesar, Ward Hill, Massachusetts) in dilute nitric acid and checking the concentration via titration with a standard 0.1 M EDTA solution (Ricca Chemical Company, Arlington, Texas). A molybdate solution was prepared by dissolving ammonium molybdate tetrahydrate powder (Alfa Aesar) in distilled water and checking the concentration via titration with a 0.05 M lead nitrate solution (Fisher). Appropriate volumes of each solution were used to synthesize the samples used in the experiments. The alpha phase material was sintered at 650ºC for 8 hours, the beta phase material was sintered at 600ºC for 8 hours, the LT gamma phase was sintered at 550ºC for 16 hours, and the HT gamma phase was sintered at 700ºC for 8 hours.

Neutron diffraction patterns were collected similarly to the LnSCF materials, however UHP hydrogen (4% in helium) was used in addition to UHP oxygen, and equal parts of gas from each cylinder were fed to the sample holder, yielding a gas atmosphere of 1% O_2, 2% H_2, 48% He, and 49% N_2. Total pressure was fixed at one atmosphere, and the same furnace and mounting hardware was used. Diffraction patterns were collected at temperatures of 300 and 400ºC. 1.599 Å neutrons were used to collect data in the d-space range of 0.55-4.15 Å. Room-temperature data was collected on the same beamline, with the samples contained in sealed vanadium cans packed under a helium atmosphere.

Synchrotron x-ray diffraction patterns were collected in the same manner as the LnSCF samples, but using 0.413227 Å wavelength x-rays. Rietveld refinements of the neutron and x-ray diffraction patterns were performed in a manner similar to the LnSCF materials.

3.3 Oxidative Coupling of Methane

Li/MgO powder was synthesized via a modified Pechini method[67]. Lithium nitrate and magnesium nitrate solutions of approximately 1 M concentration were prepared by dissolving nitrate powders (Alfa Aesar, Ward Hill, Massachusetts) in water. The magnesium nitrate solution was checked via titration with a standard 0.1 M EDTA solution (Ricca Chemical Company, Arlington, Texas), however the low valence of lithium precluded its titration, so its concentration is merely an estimate based on the weight of the starting nitrate powder. The two solutions were combined in a 1:1 ratio to create an equimolar solution of Li^+ and Mg^{2+} ions. This solution was used both for the pure Li/MgO catalyst samples as well as to create supported catalysts. Li/MgO catalyst was added to YSZ and GDC supports via incipient wetness impregnation, with a catalyst loading of 1.3 mg/m2 for Li/MgO-YSZ and 1.6-1.9 mg/m2 for Li/MgO-GDC.

HT gamma phase Bi_2MoO_6 was produced as in the previous section. PBMO was prepared via a two-step process. First, cubic, disordered PBMO was synthesized from metal nitrate solutions via a modified Pechini process as above, followed by calcination in air at 1200ºC. This produced cubic PBMO as well as a hexagonal $BaMnO_{3-\delta}$ phase. Reducing this material at 900ºC for 14 hours under an atmosphere of humidified 5% hydrogen gas in nitrogen converted the cubic, disordered PBMO and hexagonal $BaMnO_{3-\delta}$ to layered PBMO. X-ray diffraction of the resultant powder confirmed that the structure was tetragonal *P4/mmm*.

Powder samples of the materials were sieved to a 106-150 µm particle size and then loaded into quartz tubes. Reactions were carried out under temperatures ranging between 575-

850ºC, with a continuous flow of methane and oxygen fed in a 2:1 ratio. Nitrogen was used to dilute the reactants and adjust total flowrate in order to control the methane conversion. The reactor setup was operated in two modes. In the first, conversion was high (on the order of 30-40%), and the goal was to maximize C2 yield for each catalyst. In the second mode, methane conversion was kept below 10% to simulate a differential plug flow reactor, in order to compare the relative reaction rates of each catalyst. Inlet methane partial pressure varied from 0.02-0.2 atmospheres, and total flowrate varied from 20-200 mL/min. A gas chromatograph (model 8610C, SRI GC Inc.) with a HayeSep® D column and TCD detector was used to measure the outlet concentrations of hydrogen, oxygen, methane, ethane, ethylene and water, from which conversion, yield, selectivity, and reaction rates were calculated. Catalyst mass (or catalyst + support mass, in the case of Li/MgO-YSZ and Li/MgO-GDC samples) was used to normalize the rates. SiO2 particles, also sieved to a 106-150 μm particle size, were used to dilute samples in order to bring conversion below 10% for the more active materials.

4 LnSCF Perovskites

4.1 Background on SOFC Cathode Materials

The solid oxide fuel cell (SOFC) is a device that utilizes electrochemistry to convert chemical energy into electrical energy without the Carnot cycle efficiency limitations of heat engines. An SOFC has three main components: the anode, the cathode, and the electrolyte. Oxidation of the fuel occurs at the anode, which generates electrons that flow through an external circuit to reach the cathode, which consumes the electrons as a part of the reduction of oxygen that takes place on its surface. The electrolyte separates the chemical species on the anode and cathode sides of the cell, but allows O^{2-} anions to pass through it. In order to prevent short-circuiting of the cell and to maximize its power output, the electrolyte material should not conduct electrons. Figure 4-1 below shows an example fuel cell performing complete oxidation of methane and utilizing an oxygen anion conducting electrolyte material:

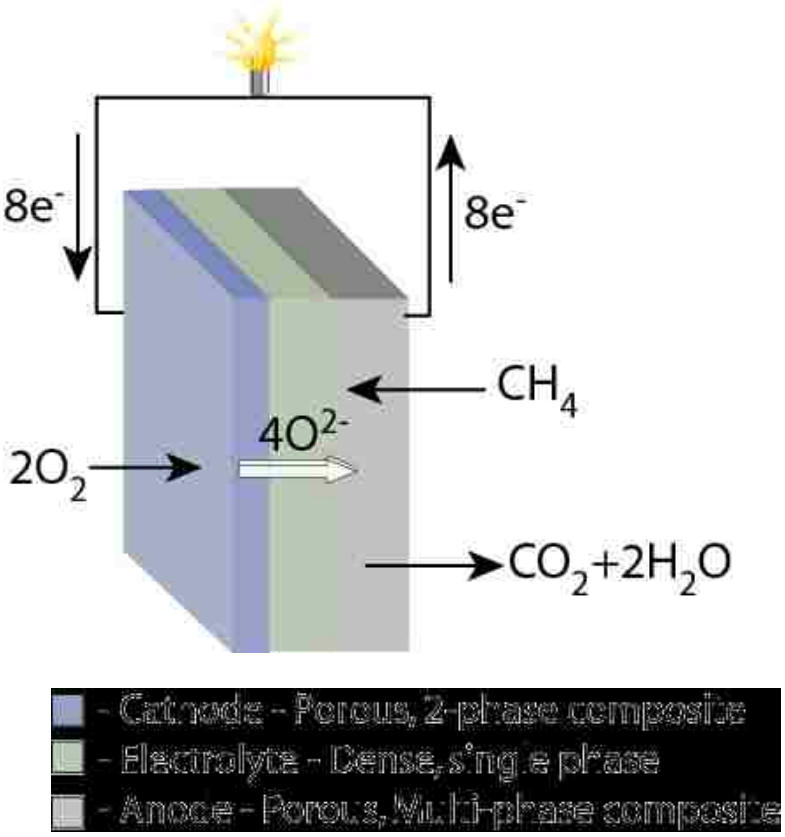

Figure 4-1 : Complete combustion reactions in a SOFC.

While methane is used in the example above, the main advantage of SOFCs is that any combustible fuel may be used, as opposed to proton conducting fuel cells, which require a proton source and are thus limited to hydrogen or methanol in terms of fuels. One of the disadvantages of SOFCs is the high temperature (>700^{0}C) required for their operation. Operation at temperatures in the 500-700ºC range would allow the use of lower cost balance of plant materials, slow the degrading effect of solid-state reactions between materials, and decrease startup and shutdown times. One limitation to operation at lower temperatures is the rate of the oxygen reduction reaction (ORR) at the cathode[72,73]. As a result, research into improving the catalytic performance of cathode materials is a highly active field.

The most promising cathode materials are the mixed ionic-electronic conductors (MIEC). Unlike purely electronic conductors, where only the catalytic sites at the triple phase boundary (TPB) of gas/cathode/electrolyte are usable, the ORR can occur at any catalytically active site on an MIEC, as the oxygen anions generated can diffuse through the MIEC bulk to the cathode/electrolyte interface[74]. This greatly increases the usable surface area of the cathode, and thus the performance. MIEC cathodes are typically *p*-type metal oxides containing a significant fraction of oxygen vacancies that facilitate the rapid transport of oxygen anions via a vacancy hopping mechanism. Example materials include perovskites of the form ABO_3, layered perovskites of the form $AA'B_2O_{6-\delta}$, and Ruddlesden-Popper phases of the form $A_{n+1}B_nO_{3n+1}$.

The electrical conductivity of these materials is typically significantly higher than the ionic conductivity. As such, the rate limiting process in the cathode is generally considered to be either the surface oxygen incorporation rate, or the bulk oxygen anion transport rate. It has previously been proposed that there is a link between the measured surface and bulk functional properties of these materials are linked. This hypothesis is based on an observed correlation between the measured bulk ionic transport (measured as a diffusivity, *D*) and surface oxygen exchange kinetics (typically measured as a surface exchange coefficient, *k*)[75–77]. Experimental data points for *k* and *D* from a number of studies appear to cluster into two groups depending only on whether electronic or ionic conductivity is dominant. This suggests a powerful and fundamental link between bulk and surface properties where the mobility of an oxygen anion in the bulk is related to the rate of oxygen dissociation on the surface. While this link was hypothesized almost twenty years ago, we currently have no fundamental understanding of what this link is, and there is an underlying unanswered question: Why would the dissociation of oxygen on the surface be correlated to the motion of oxygen within the bulk?

Ascertaining the source of this proposed link first depends on the accurate determination of all of the relevant properties. k and D are typically determined by isotope exchange depth profiling (IEDP) or conductivity relaxation experiments. In both cases, both parameters are fit to a single exponential decay, a procedure where the reported values can depend strongly on the fitting approach[78]. Other experimental problems can strongly influence these values. For example, the models used to determine k and D from IEDP depend strongly on the assumptions and boundary conditions, and there can be significant deviation of the actual conditions from those assumed[79]. Additionally, the surface composition of these materials is commonly reported to differ significantly from the bulk[78,80–82]. All of these issues lead to significant scatter in experimentally reported values these parameters in the literature. For example, the surface exchange rate for $La_{0.6}Sr_{0.4}Co_{0.2}Fe_{0.8}O_{3-\delta}$ varies by an order of magnitude between similar studies[83,84].

This work seeks to address these issues by utilizing a combination of techniques to study the bulk oxygen mobility and surface oxygen exchange rate independently. We study a set of three perovskite structure materials, $Ln_{0.5}Sr_{0.5}Co_{0.8}Fe_{0.2}O_{3-\delta}$, where Ln represents La, Pr, and Nd. *In-situ* neutron powder diffraction is utilized to quantify the oxygen mobility in terms of the thermal displacement parameter for the oxygen anions. The surface exchange rate is determined by a pulsed isotopic transient technique that aims to determine the equilibrium oxygen exchange rate independent of bulk transport. The surface composition is determined by X-Ray Photoelectron Spectroscopy (XPS). All of this data is then utilized to interpret the electrochemical performance of these materials as SOFC cathodes and to support the observed link between *k* and *D*.

4.2 Results

4.2.1 LnSCF Structure Determination

Neutron powder diffraction patterns were collected for LSCF, NSCF and PSCF at room temperature and at high temperature, 527-827ºC, at pO_2 = 10^{-1} atm. Patterns were also collected for LSCF at pO_2=10^{-2} and 10^{-3} atm. Beam time allocation limitations restricted data collection on NSCF and PSCF to the single pO_2. Synchrotron XRD data was collected at room temperature for all samples. No impurity phases were detected in any of the samples in this study.

The room temperature XRD and NPD data for LSCF were best fit to an $R\bar{3}c$ space group, with lattice parameters a = b = 5.4367 Å and c = 13.2556 Å. Refinement of the neutron data collected for LSCF between 520-827ºC at a pO_2 between 10^{-3} and 10^{-1} atm showed that the structure transforms to $Pm\bar{3}m$ symmetry in this temperature-pO_2 range, with lattice parameters a = b = c = 3.8721 to 3.9071 Å. Figure 4-2a shows the neutron powder diffraction pattern for LSCF measured at 827ºC at a pO_2 of 10^{-1} atm, and the Rietveld refined fit to the $Pm\bar{3}m$ space group with quality of fit parameters χ^2 =2.015, and R_{WP}= 3.21%. Corresponding structural parameters from Rietveld refinements for this and all other neutron diffraction patterns at 827ºC are reported in Table 4-1.

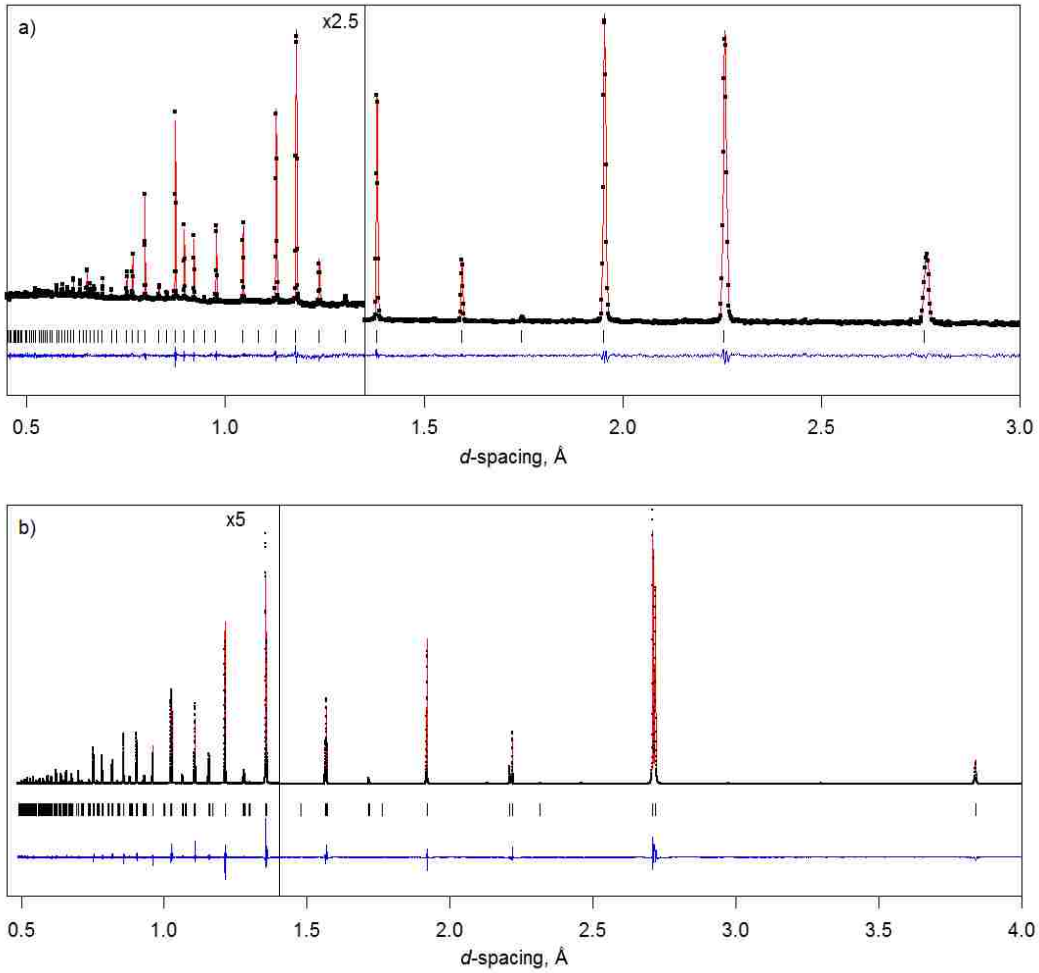

Figure 4-2 : (a) Neutron powder diffraction pattern for LSCF at 827ºC under a pO_2 of 10^{-1} atm ($Pm\bar{3}m$), and (b) synchrotron x-ray powder diffraction pattern for the same sample at room temperature in air ($R\bar{3}c$). Patterns consist of observed intensities (dots), calculated intensities (red, upper line), observed-calculated intensities (blue, lower line), and Bragg reflections (vertical tick marks). The low d-spacing portion of each pattern has been magnified in the vertical direction by the multiplier shown. Peaks at 2.13 & 2.46 Å correspond to a 0.9 wt% CoO impurity in the material, and the peak at 2.97 Å corresponds to a 0.1 wt% La_2O_3 impurity.

	LSCF 10^{-1} atm pO_2	LSCF 10^{-2} atm pO_2	LSCF 10^{-3} atm pO_2	PSCF 10^{-1} atm pO_2	NSCF 10^{-1} atm pO_2
Space group	Pm$\bar{3}$m	Pm$\bar{3}$m with split O sites	Pm$\bar{3}$m with split O sites	Pm$\bar{3}$m	Pm$\bar{3}$m
a=b=c (Å)	3.90320(2)	3.90602(2)	3.90713(2)	3.88957(2)	3.88449(3)
Oxygen content	2.81(1)	2.77(1)	2.78(1)	2.84(1)	2.75(2)
χ^2	2.015	1.964	2.056	1.800	1.754
R_{wp}	3.21%	3.29%	3.32%	3.72%	3.18%
O (x)	0.5	0.540(6)	0.546(3)	0.5	0.5
Atomic displacement parameters (Å^2) × 100					
Ln/Sr, U_{iso}	2.86(2)	3.02(2)	2.98(2)	3.21(3)	3.28(3)
Co/Fe, U_{iso}	1.77(2)	1.83(3)	1.83(3)	1.75(3)	1.87(3)
O, U_{11}	5.19(3)	4.72(58)	4.26(37)	6.55(4)	7.08(5)
O, U_{22}	5.19(3)	3.69(31)	3.39 (25)	6.55(4)	7.08(5)
O, U_{33}	2.03(4)	2.04(4)	2.04(4)	2.20(4)	2.21(5)

Table 4-1: Rietveld fit parameters for the materials at 827ºC. A-site cations are located at Wyckoff position 1a (0, 0, 0) and B-site cations are located at Wyckoff position 1b (½, ½, ½). Oxygen is located at Wyckoff position 3c (½, ½, 0) in the base model and 12h (x, ½, 0) in the split oxygen site model.

Similar Rietveld refinements were performed for NPD patterns of PSCF and NSCF collected at room temperature and between 520-827ºC at a pO_2 of 10^{-1} atm. Both materials were cubic, Pm$\bar{3}$m space group, at and above 625ºC but reverted to *R*$\bar{3}$*c* at, and below, 520ºC.

The room temperature synchrotron patterns for the PSCF and NSCF patterns were each fit with a mixture of two phases: trigonal *R*$\bar{3}$*c* and orthorhombic *Pnma*. A Representative room temperature synchrotron XRD pattern for LSCF with corresponding Rietveld refined fit to space group R$\bar{3}$c is shown in Figure 4-2b. Corresponding structural parameters for the synchrotron XRD data are provided in Table 4-2.

	LSCF	PSCF (phase 1)	PSCF (phase 2)	NSCF (phase 1)	NSCF (phase 2)
Space group	R$\bar{3}$c	R$\bar{3}$c	Pnma	R$\bar{3}$c	Pnma
Weight fraction	1	0.52	0.48	0.16	0.84
a (Å)	5.43670(1)	5.42139(1)	5.39099(3)	5.41200(7)	5.38121(1)
b (Å)	5.43670(1)	5.42139(1)	7.61885(3)	5.41200(7)	7.60651(1)
c (Å)	13.25555(1)	13.15816(3)	5.43564(2)	13.14912(21)	5.43092(1)
$\chi 2$	4.873	5.629	5.629	4.208	4.208
Rwp	14.1%	14.2%	14.2%	10.7%	10.7%

Table 4-2: Rietveld fit parameters for synchrotron powder XRD of the materials at room temperature.

We have utilized this combination of NPD and synchrotron XRD to determine if cation ordering occurs in these materials; this can be difficult to detect in a typical laboratory XRD pattern. NPD and XRD are required due to the similar diffraction properties of either neutrons or X-rays for some of the elements. For example, the neutron scattering power of an atom depends on its coherent scattering length, *b*[85]; 7.02, 8.24, 4.58, 7.69, 2.49, and 9.45 fm for Sr, La, Pr, Nd, Co, and Fe, respectively[86]; NPD cannot distinguish between ordered and disordered A-site structures due to the similar scattering lengths of La, Nd, and Sr. In contrast, Co and Fe have very different scattering lengths, and any ordering of the B sites would be quite apparent in the neutron data. The situation is reversed in the case of XRD, where scattering power is influenced by the form factor, *f*, of an atom[85], which correlates with the atomic number. In this situation, Co and Fe are difficult to distinguish (f_1 of 27.3 vs 26.3 for 30 keV x-rays), but Sr is very different from La, Pr, and Nd (f_1 of 38.4 vs 56.2, 58.4, and 59.5 for 30 keV x-rays[87]). Thus, synchrotron XRD data was used to investigate A site ordering, and NPD data was used to investigate B site ordering.

Attempts were made to fit both the XRD and NPD data to models with rock salt, layered, and columnar ordered A and/or B-site cations (Fm$\bar{3}$m, P4/mmm, $P2_1/m$, and $P4_2/nmc$)[88], but all

the models tested generated extra peaks in either the NPD or XRD data, due to additional lattice planes, that were not observed and these more complex models did not improve the fit. Thus, we conclude that no cation ordering exists in LSCF under the conditions tested, confirming prior work on related materials[89,90].

4.2.2 Refinement results

Figure 4-3 shows the lattice parameters, oxygen stoichiometry, and the oxygen anisotropic atomic displacement parameters for all of the high temperature data for LSCF, PSCF and NSCF. Comparing data at pO_2=10^{-1} atm, Figure 4-3a, the lattice parameter increases with increasing temperature for all materials due to both thermal and chemical expansion. The total expansion coefficients for the materials were calculated to be 28×10^{-6}, 29×10^{-6}, and 30×10^{-6} for LSCF, PSCF, and NSCF, respectively. At each temperature, the lattice parameter decreases in the order LSCF>PSCF>NSCF, in agreement with the expected trend from the Shannon radii[91].

Similarly, the lattice parameter increased with decreasing gas phase pO_2 for LSCF, Figure 4-3a; at 625ºC the lattice parameter was 3.88114(1), 3.88981(2), and 3.89210(1) Å at a pO_2 of 10^{-1}, 10^{-2}, and 10^{-3} atm, respectively. The smaller increase observed for the second decrease in order of magnitude of pO_2 may be indicative of a lack of equilibration of the sample[24], as full equilibration at low pO_2 can be difficult to obtain in limited beam time. This chemical expansion is due to the reduction of B-site cations, as evidenced by the corresponding decrease in oxygen stoichiometry with decreasing pO2, Figure 4-3b. The coefficient of chemical expansion (fractional increase in lattice parameter per decrease in fractional oxygen occupancy)[92,93] for LSCF was calculated to be 6.4%. Subtracting this chemical expansion from the thermal expansion for LSCF yields a purely thermal expansion coefficient of 22×10^{-6}.

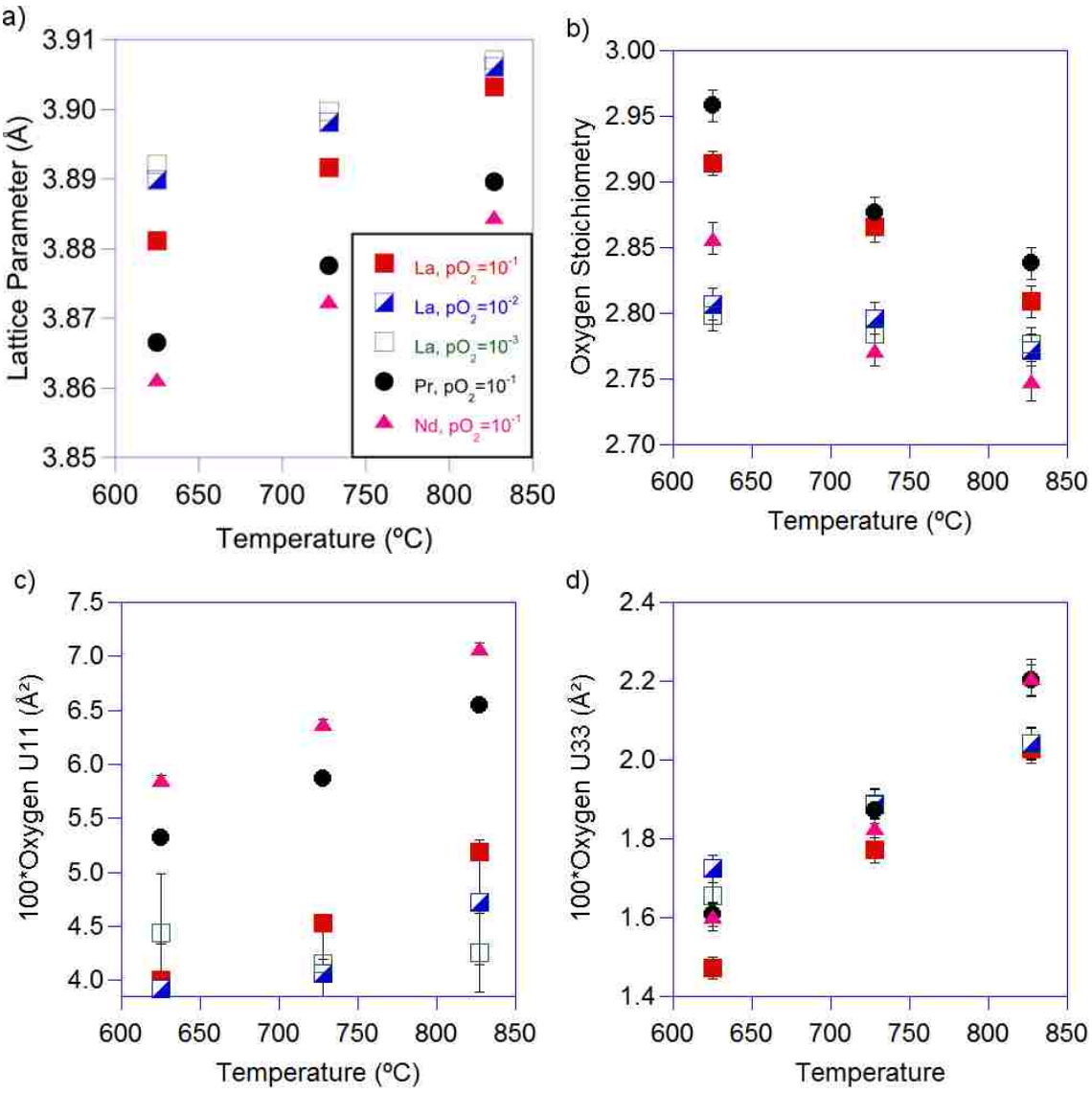

Figure 4-3 : (a) Lattice parameter $a = b = c$ (Pm$\bar{3}$m), (b) oxygen stoichiometry, (c) oxygen displacement parameter U_{11}, and (d) oxygen displacement parameter U_{33} as a function of temperature and sample. Squares represent LSCF, circles PSCF, and triangles NSCF. The filling of shapes denotes the oxygen partial pressure that the sample was measured under: 10^{-1} atm (filled), 10^{-2} atm (half-filled), and 10^{-3} atm (empty). Error bars represent standard deviations for parameter values calculated via Rietveld refinement.

Our primary interest in performing *in-situ* NPD as opposed to XRD is the relatively strong interaction of neutrons with oxygen nuclei and ability to obtain high quality data in regions of high momentum transfer, Q. These factors are utilized to obtain the position,

anisotropic displacement, and occupancy of cations, and especially oxygen anions, in the materials in order to provide insight into possible O^{2-} transport pathways.

The atomic displacement parameters for the cations were refined from the NPD data isotropically for all samples under all conditions, as no preferred displacement direction was observed and the quality of fit was not significantly improved by utilizing anisotropic displacement parameters. Furthermore, all cations occupying the same site were constrained to share a single displacement parameter for each temperature, pO_2, and material. This was necessary to ensure a stable refinement due to the random arrangement of the different A and B-site cations: an increase in the displacement parameter of a cation with a corresponding decrease in displacement parameter for the other cation on the same site will lead to many equivalent solutions to the least squares minimization routine involved in Rietveld refinement. Thus, it is common practice to model crystallographically similar atoms as having shared displacement parameters[94]. At 827ºC, A-site cation displacements ranged from 2.86-3.28 $x10^{-2}$ $Å^2$, and B-site cation displacements ranged from 1.75-1.87 $x10^{-2}$ $Å^2$, Table 1. Displacements increased with temperature, as may be expected due to increased lattice vibration.

The oxygen stoichiometry for NSCF was significantly lower than for LSCF and PSCF at the same temperature and pO2, Figure 4-3b; 2.75(2) for NSCF at 827ºC and $pO_2=10^{-1}$ atm, compared with 2.84(1) and 2.81(1) for PSCF and LSCF, respectively. As expected from reduction of B-site cations, the oxygen stoichiometry generally decreased with increasing temperature, and for LSCF, with decreasing pO2, Figure 4-3b. As with the lattice parameter, the smaller shift in oxygen stoichiometry of LSCF between pO_2 of 10^{-2} and 10^{-3} atm may be due to a lack of equilibration of the sample.

The anisotropic atomic displacement parameters for oxygen across the face of the Pm3̄m unit cell were significantly higher for PSCF and NSCF when compared to LSCF across all

temperature and pO_2 measured, Figure 4-3c. This is interpreted as corresponding to greater oxygen mobility in NSCF and PSCF. As we have previously reported for the Ba analog of these materials, atomic displacement towards the central B-site cation in the unit cell is significantly lower, and does not vary significantly between materials or with pO_2, Figure 4-3d. This anisotropy makes sense when one considers the curved pathway of oxygen transport between nearest neighbor oxygen sites that has been proposed for cubic perovskites[95].

GSAS was utilized to generate observed Fourier maps of nuclear density from the NPD data at 827ºC and $pO_2=10^{-1}$ atm to aid in visualization of oxygen anion displacement, Figure 4-4. The NSCF and PSCF samples both showed anisotropic displacement of the oxygen site along the face of the unit cell, Figure 4-4; $U_{11}=U_{22}$ were $7.08(5)\times10^{-2}$ and $6.55(4)\times10^{-2}$ Å^2 and U33 was $2.21(5)\times10^{-2}$, $2.20(4)\times10^{-2}$ Å^2 at 827ºC and $pO_2=10^{-1}$ atm for NSCF and PSCF, respectively.

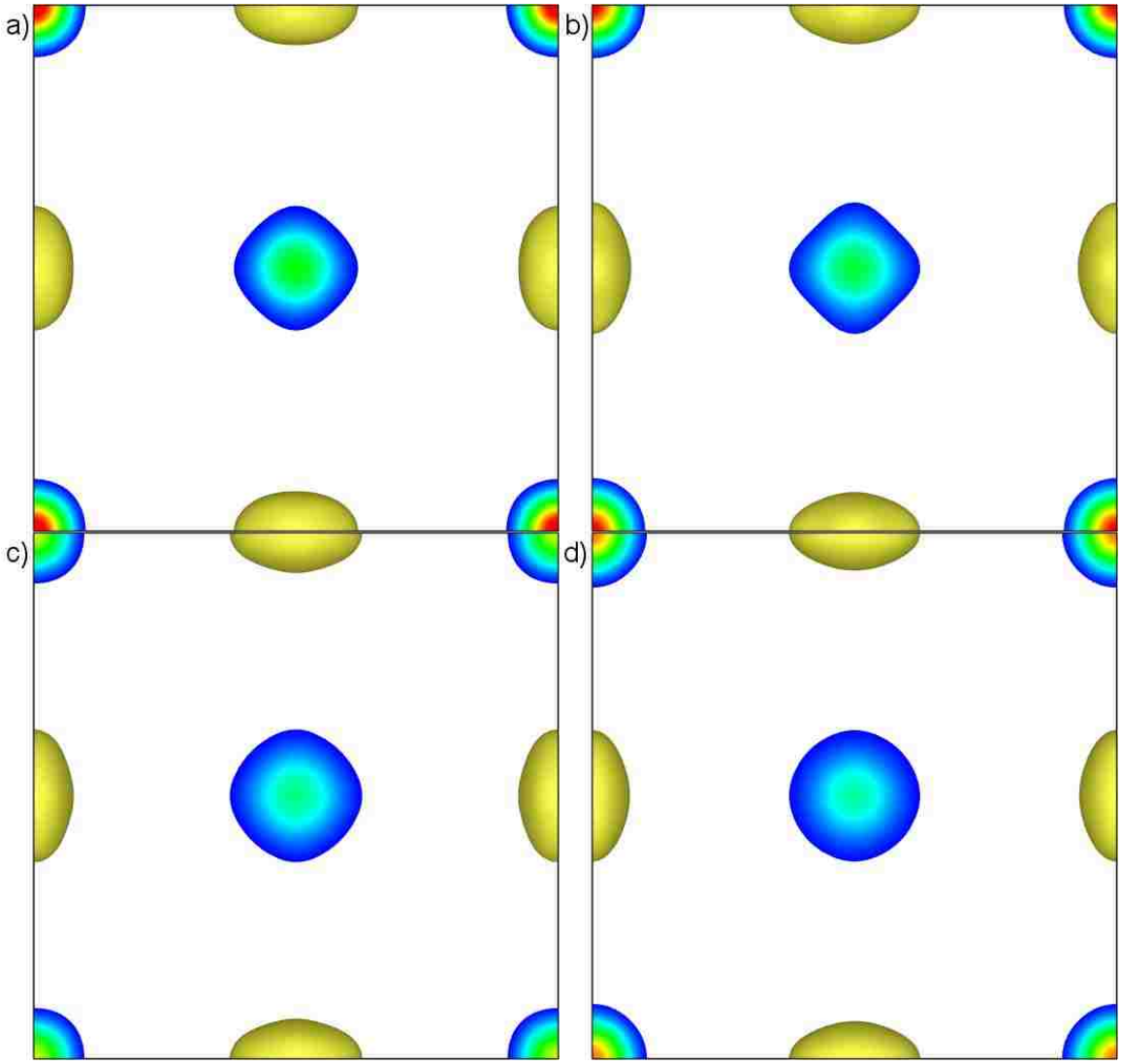

Figure 4-4 : Observed Fourier maps of nuclear density at 827ºC, as viewed perpendicular to the (100) plane, for (a) LSCF under a pO_2 of 10^{-1} atm, (b) LSCF under a pO_2 of 10^{-3} atm, (c) PSCF under a pO_2 of 10^{-1} atm, and (d) NSCF under a pO_2 of 10^{-1} atm. A-site cations are shown at the corners of the unit cell, and oxygen anions are shown at the edges and in the center. B-site cations are obscured by the oxygen.

The corresponding displacement parameters for LSCF were $U_{11}=U_{22}=5.19(3)x10^{-2}$ Å^2 and U_{33} = 2.03(4)x10^{-2}; however, the observed shape of the nuclear density for the oxygen site was not a simple ellipsoid, but was cross-shaped, parallel to the edge of the unit cell and pointing in between the A-site cations, Figure 4-4a. This anisotropic 'shape' became more pronounced at lower oxygen partial pressures, Figure 4-4b. Consequently, the neutron powder diffraction data for LSCF was fit using a modified version of the Pm$\bar{3}$m model that moved the oxygen atom off

the 3c Wyckoff position, creating four oxygens at 12h positions at equal distances from the original 3c site, (±x, ½, 0) and (½, ±x, 0), in order to more accurately reflect the cross-like oxygen nuclear density. This change to the model more accurately represents the shape of the nuclear density but does not significantly change the quality of fit to the data. Average χ^2 of the 10^{-2} and 10^{-3} atm pO_2 LSCF NPD data slightly decreases from 2.560 to 2.543. A visualization of the difference between this modified model and a standard $Pm\bar{3}m$ perovskite model can be seen in Figure 4-5. The oxygen occupancy refined to very nearly one quarter of the value in the un-split model, such that stoichiometry change was within error, e.g. for LSCF at 827ºC under a pO_2 of 10^{-3} atm, the fractional occupancy of oxygen decreased from 0.927(3) to 0.926(4) (4 x 0.231(1)) after splitting the site in the model. The position x was also refined in this model.

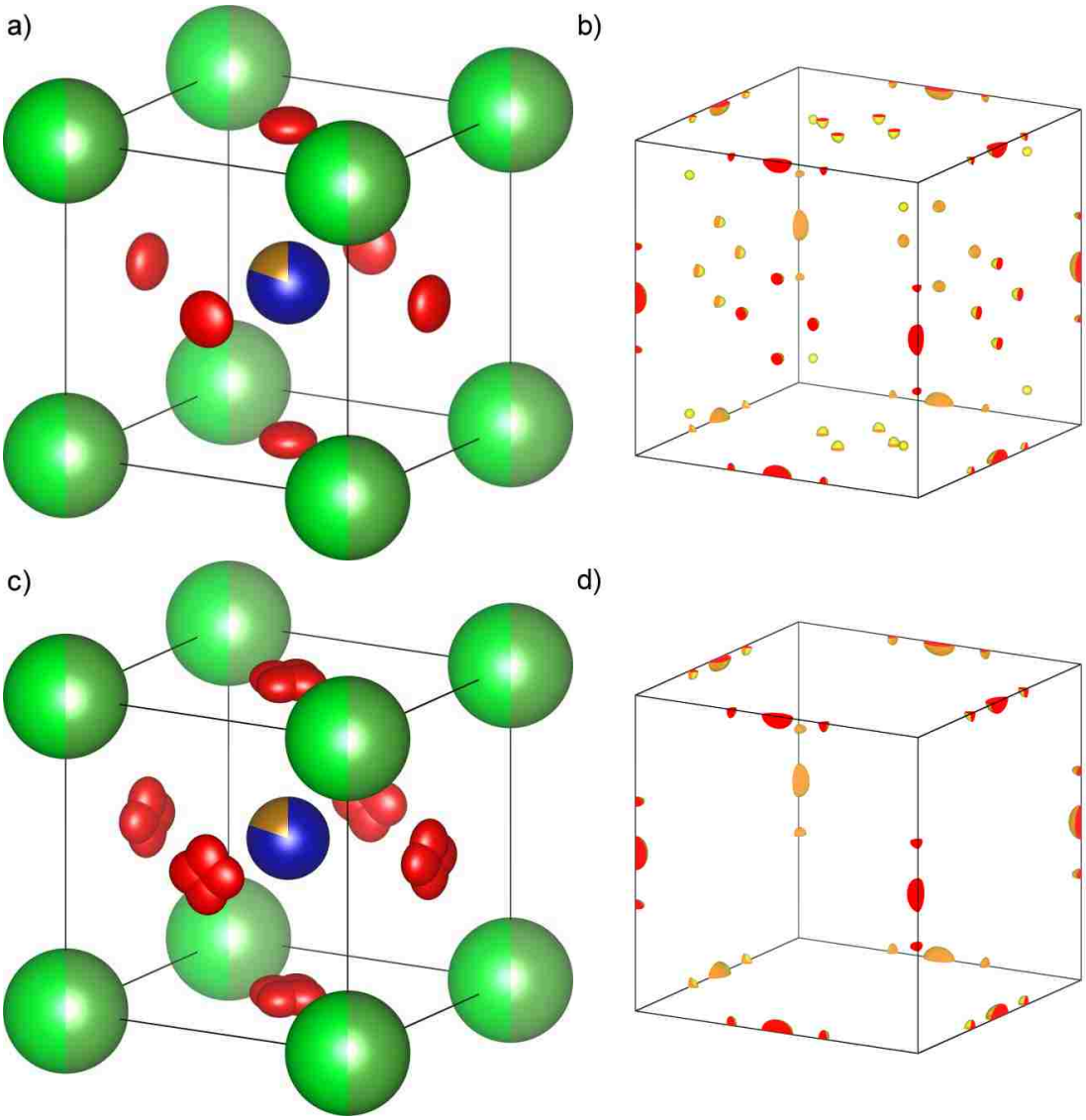

Figure 4-5 **:** Visualization of LSCF using (a) the Pm3̄m model, (b) a Fourier difference map for the Pm3̄m model, (c) the Pm3̄m model with split oxygen sites, and (d) a Fourier difference map for the Pm3̄m model with split oxygen sites. The red and yellow volumes in the difference map represent nuclear density that is underrepresented by the model. The improved fit of the model in (c) translates into more accurate representation of the nuclear density of the oxygen sites.

4.2.3 LnSCF X-ray Photoelectron Spectroscopy

The results of the XPS analysis are summarized in Table 4-3. There is an enrichment of cobalt near the surface at the expense of iron for all of the materials. This has been observed in other studies[96,97]. In contrast to other literature, we found no significant enrichment of

strontium for LSCF or NSCF and only slight enrichment for PSCF. Prior reports have shown mixed results for the surface concentration of strontium for related LSCF, LSC and LSM perovskites, with some researchers showing an enrichment on the surface[96,98–102] and others showing identical or decreased strontium/lanthanide ratios on the surface, relative to the bulk[96,97,101], often in the same experiment. The lack of observed strontium surface enrichment could be due to the fact that the XPS technique used in this paper averages crystal composition across several layers. However, many of the reported results for strontium enrichment were for perovskites grown as thin films, such as that performed by Crumlin et al[101], which showed a surface enriched in strontium for a thin film LSC sample, but no such enrichment for pellets synthesized from LSC powder. This indicates that segregation of strontium at the surface is perhaps a function of the synthesis method, rather than the composition. Sodium was also observed on all three samples, despite its absence in the XRD and NPD data. Sodium is a known impurity in the iron nitrate used to synthesize the materials in this study, at a level of less than 0.05%, and segregation of impurities to the surface has been observed by others[102,103], which can lead to significant surface quantities despite only being present in trace amounts in the bulk.

Element	Bulk	LSCF	PSCF	NSCF
Ln	10	8.5	6.2	9.6
Sr	10	8.6	8.7	7.7
Co	16	10.4	16.7	12.4
Fe	4	0.4	0.4	0.4
O	60	64.3	63.7	62.5
Na	0	7.8	4.3	7.3

Table 4-3: concentrations in mole percent, as determined by XPS, versus the bulk composition.

4.2.4 LnSCF Pulsed Isotopic Oxygen Exchange & Electrochemical Impedance Spectroscopy

Isotopic oxygen exchange rates for the PSCF and NSCF materials were observed to be nearly two orders of magnitude higher than that of LSCF. For example, at 750ºC exchange rates for PSCF and NSCF were 6.1×10^{-4} and 5.6×10^{-4} mol·m^{-2}·s^{-1}, respectively, and 1.7×10^{-5} mol·m^{-2}·s^{-1} for LSCF. An Arrhenius plot of the surface exchange rate, normalized for surface area is shown in Figure 4-6. All three materials show linear trends. BET surface areas of the materials were 1.2 m^2/g for LSCF, 0.18 m^2/g for PSCF, and 0.42 m^2/g for NSCF, and activation energies were calculated to be 221 ± 4, 146 ± 6, and 161 ± 9 kJ/mol for LSCF, PSCF, and NSCF, respectively.

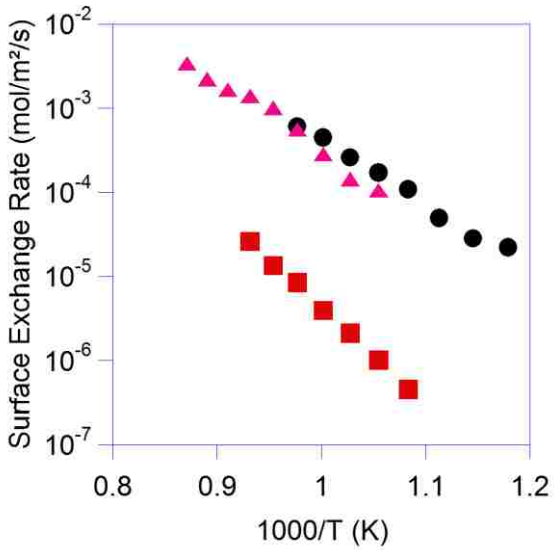

Figure 4-6 : Oxygen surface exchange rate as calculated from pulse isotopic oxygen exchange. Squares represent LSCF, circles PSCF, and triangles NSCF.

Similar to the oxygen exchange experiments, the PSCF, and NSCF materials showed improved performance relative to LSCF when used as air electrodes for symmetrical solid oxide electrochemical cells. The area-normalized polarization resistance across the 400-700ºC range is plotted against inverse temperature in Figure 4-7. A distinct change is slope is observed at

~550ºC for all of the materials. We attribute this to the observed change of phase from R3̄c to Pm3̄m between 520-625ºC observed in the NPD data for PSCF and NSCF materials. A similar transition exists for the LSCF between 520ºC and room temperature.

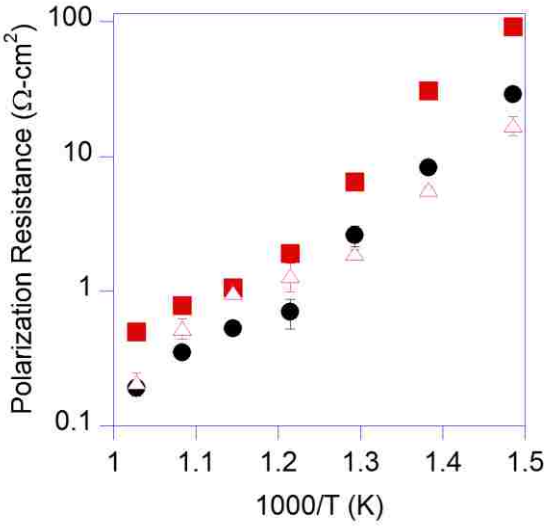

Figure 4-7 : Area specific polarization resistance of symmetric cells made from the three materials, as measured by EIS. Squares represent LSCF, circles PSCF, and open triangles NSCF.

These impedance measurements were repeated utilizing Ag as a contact paste material with a sintering temperature of 1200ºC. While the absolute values of polarization were lower than with Pt paste, possibly due to some catalytic effect of the Ag, the overall trend of performance with composition was maintained. Furthermore, the microstructure of these two samples is likely significantly different due to the different sintering temperatures. While differences in cell impedance can be caused by differences in microstructure, we believe that the repetition of this trend across four samples per material (two at each sintering temperature) indicates a true functional difference between the materials, with a polarization resistance trend of LSCF>NSCF≥PSCF.

The scale of Figure 4-7 somewhat masks the significant increase in polarization resistance between the samples. In general, the polarization resistance for LSCF was 1-2 times that of NSCF and 2-3 times that of PSCF. Representative Nyquist plots are shown for three representative samples at 600ºC and 700ºC in Figure 4-8. All of the data was confirmed by measuring multiple samples of each material. The large, semicircular arc of each spectrum represents the polarization resistance of the electrodes of each cell, and the differences between the materials are clearly visible at 700ºC. The polarization resistance for LSCF electrodes was 500 mΩ·cm^2 compared with 190 mΩ·cm^2 for PSCF and 210 mΩ·cm^2 for NSCF electrodes at 700ºC. At 400ºC we measured 92 Ω·cm^2 for LSCF electrodes compared with 29 and 17 Ω·cm^2 for PSCF and NSCF electrodes, respectively.

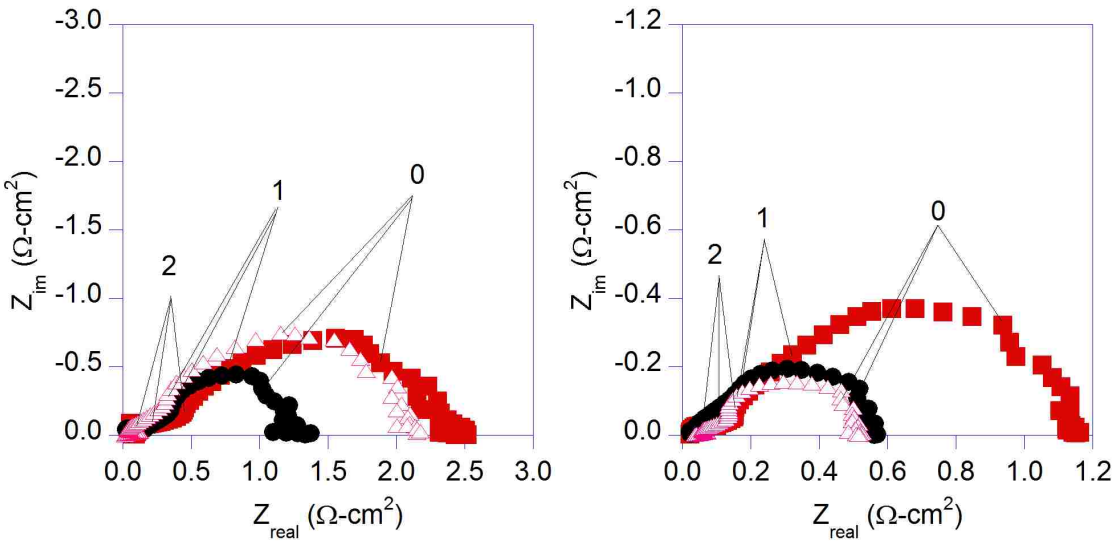

Figure 4-8 : Example Nyquist plots of impedance spectra for samples at (a) 600ºC and (b) 700ºC. Electrolyte resistance was subtracted, and data was normalized by electrode area. Squares represent LSCF, circles PSCF, and open triangles NSCF. Data shown is for the better of the two cells tested for each of the three electrode materials. Numerals represent the log of the AC frequency of the indicated data point in Hz.

4.3 Discussion

Decreasing oxygen stoichiometry with decreasing lanthanide size has been observed in other perovskites[104–107]. We observe the same trend when comparing LSCF and NSCF, the smaller Nd cation leads to lower oxygen stoichiometry. However, the PSCF sample had an oxygen stoichiometry very close to that of LSCF, rather than a value in between the LSCF and NSCF as may be expected from the cation radius. The related material, $Pr_{0.5}Sr_{0.5}CoO_{3-\delta}$, was reported[108] to have an oxygen stoichiometry of about 2.85 at 700ºC under a pO_2 of 10^{-1} atm, which is close to the value of 2.88(1) obtained from the NPD data for PSCF at 728ºC under the same partial pressure of oxygen. This suggests that the value we have determined is correct. Despite this, data in the literature on the stoichiometry of other Pr containing perovskites contains mixed results, with some groups observing a stoichiometry closer to La rather than Nd analogues[104], and others reporting the reverse[106]. This unpredictable behavior may be due to the availability of a +4 oxidation state for the Pr ion, which would allow Pr based structures to compensate for aliovalent doping on the A-site without the need to generate oxygen anion vacancies, which may explain a higher oxygen stoichiometry than implied by cation size arguments.

As a first approximation, we may expect that increasing oxygen mobility would directly correlate with decreasing oxygen stoichiometry. However, *in-situ* neutron diffraction provides an even greater level of detail as we look at atomic displacement. The increased oxygen atomic displacement in the U_{11}/U_{22} directions for NSCF when compared to LSCF follows naturally from the observed increase in oxygen vacancy concentration for NSCF. An increase in vacancy concentration would be expected to lead to an increase in oxygen hopping between sites, and thus increase in average displacement along the hopping pathway. We would also expect

increased oxygen displacement due to the increased free lattice volume of NSCF compared to LSCF. The decrease in average A-site Shannon radius is greater than the decrease in lattice parameter[91]. Thus there is more free volume in the unit cell of NSCF, a 'wider' pathway, for the oxygen anions to hop between sites.

PSCF and LSCF have similar oxygen stoichiometry but very different atomic displacement. Additional lattice volume is likely the origin of the increased U_{11}/U_{22} displacement in PSCF compared to LSCF, which have similar oxygen stoichiometry. The lack of a trend for the U_{33} direction, representing motion towards the B-site, is likely due to the fixed B-site composition across all samples and is representative of the relatively small motion of the oxygen anion in that direction during oxygen site hopping[95]. Based on all of these considerations, we propose that the oxygen anion mobility of these materials would follow the trend NCSF ≥ PSCF > LSCF.

A cross shape in the nuclear density of oxygen determined for La was also observed by Yashima[10] for $La_{0.6}Sr_{0.4}Co_{0.8}Fe_{0.2}O_{3-\delta}$ at 1260ºC in air. Elevated temperatures are reducing, similar to low pO_2 atmospheres, so there is a trend that the cross shape is more visible as the concentration of oxygen vacancies increases. This shape could be due to increased vibration of oxygen towards vacant sites and/or increased oxygen hopping between sites. The NSCF material had a similar number of oxygen vacancies but no cross shape to the oxygen nuclear density, but it may have been masked by increased freedom of motion towards the A-sites: the decrease in average A-site radius (over 3%)[91] was greater than the observed decrease in lattice parameter (0.2-0.5%), when compared with the LSCF material.

The results of the pulse isotopic oxygen exchange showed that the PSCF and NSCF materials were over an order of magnitude more reactive than LSCF in terms of surface oxygen exchange. This higher activity is also reflected in the EIS results, and thus performance in an

SOFC cathode. The question then arises as to the cause of these differences. It is critical to understand how the bulk composition of these materials influences this surface exchange rate.

Differences in crystal structure or deviations from expected bulk compositions could cause performance differences. The bulk composition of all of these materials, as determined by XRD and NPD, were confirmed to be in the expected ratios of 5:5:8:2 for the lanthanide, strontium, cobalt, and iron cations, respectively, and all three samples were observed to be cubic Pm$\bar{3}$m in the temperature range of 625-827ºC.

An alternative explanation is that the surface exchange rate is dictated by differences in surface composition. As has been reported by numerous authors[96–102], the surface composition of SOFC cathode materials can differ markedly from the bulk due to surface enrichment of one or more elements, typically enrichment of Sr. 'Surface' is a relative term that may refer to the very outermost layer of cations or it may include a short distance away from the surface; it can be difficult to draw a line on where a technique is surface sensitive. Here we generally consider the surface to include a short distance (~10 nm) into the bulk, as may be probed with XPS. While the surface composition measured by XPS differed from the bulk for all three materials, all three showed the same Co/Fe ratio enrichment, and none showed significant surface enrichment of strontium. Another possibility for the difference in observed surface exchange rate is then that the presence of the different A-site cations, La, Nd, or Pr, on the surface influences the rate; however, numerous studies have demonstrated that the B-site transition metal cations typically control the reaction rate over perovskites[109,110].

It is possible that the difference in EIS performance between symmetric cells is due to a difference in microstructure between the samples. However, there are a few reasons why this may not be the case. Firstly, the cells were fabricated in an identical manner, so the electrodes should have similar microstructures. Secondly, the plot of impedance versus inverse

temperature shows a change in slope for all tested samples, and this change occurs in the same temperature range as a phase change in the electrode materials from $R\bar{3}c$ to $Pm\bar{3}m$. This implies that the performance of the cells is a function of the crystal structure rather than the microstructure. Thirdly, the EIS performance data has the same trend as the oxygen isotope pulsing data, which are independent of microstructure.

The only trend that we find correlates with the observed surface exchange rate and the electrode impedance is the trend in oxygen mobility determined from the neutron diffraction data. Thus, for this set of materials, it appears that the proposed link between surface exchange and bulk transport is correct. Rapid bulk transport and surface exchange then lead to low electrochemical impedance when the material is employed as an electrode. The remaining question is the source of this correlation.

Following oxygen dissociation on the outermost MIEC material surface, an available vacant lattice site is necessary for incorporation of the oxygen anions into the bulk. These vacant sites are regenerated by oxygen anion transport from the surface through the bulk. Thus, if we consider that regeneration of vacant surface sites can be rate-determining, it follows that rapid, near-surface, bulk oxygen transport facilitates more rapid oxygen incorporation.

If we consider other possible rate determining steps, such as oxygen dissociation on the surface, we require a more fundamental correlation between the factors that limit oxygen transport and the energetics of these other steps. Certainly factors such as variations in lattice parameter with vary A-site cation radius directly influences oxygen anion transport and will alter the distance between surface catalytic sites for oxygen dissociation. We assume that two metal sites are necessary for dissociative adsorption of O_2.

5 Bismuth Molybdates

5.1 Introduction

Acrolein is an important precursor to a wide variety of fine chemicals, and is commercially produced via the partial oxidation of propylene:

$$C_3H_6 + O_2 \rightarrow C_3H_3OH + H_2O$$

One class of catalysts commonly used for this reaction is the bismuth molybdate family[111]. Partial oxidation reactions over these catalysts are believed to proceed via a Mars van Krevelen mechanism[112–115], so oxygen mobility and conductivity may be key components to their activity, in the same vein as SOFC cathode materials. As a result, the technique of neutron powder diffraction was utilized to probe the structure of various bismuth molybdate materials in search of features that may be linked to oxygen mobility, such as localized vacancies or strained bonds.

The major phases of the bismuth molybdate materials have a chemical formula of the form $Bi_2(MoO_3)_nO_3$, with n=1, 2, or 3. This yields three compositions and four distinct phases: alpha (n=3), beta (n=2), and two different polymorphs of the gamma (n=1) phase, low temperature (LT gamma) and high temperature (HT gamma). LT gamma undergoes an irreversible transition to HT gamma at 604ºC[71], which allows for its analysis under the same conditions as the LT gamma phase.

This work focuses on the localization of oxygen vacancies in these materials, as well as the relative thermal displacement parameters for different oxygen sites in each phase. In

previous work by our laboratory, we observed that, in other oxide materials, such properties are linked with oxygen conductivity and the ability of those materials to incorporate and release oxygen at the surface[70,116,117].

5.2 Results and Discussion

Neutron diffraction patterns for the four materials at 400ºC are shown in Figure 5-1, and a summary of the refinement parameters for each phase is shown in Table 5-1. The alpha and HT gamma phases have monoclinic $P2_1/c$ structures, the beta phase is also monoclinic, with $P2_1/n$ symmetry, and LT gamma is orthorhombic with a $Pca2_1$ structure. All four samples were high purity: the alpha and LT gamma phase samples had no detectable impurity peaks in the neutron diffraction patterns, and the beta and HT gamma phase samples only had impurity concentrations of 2.7 wt% and 3.0 wt%, respectively. In the case of the beta sample, the impurity was an HT gamma phase, and in the case of the HT gamma sample, the impurity was bismuth oxide.

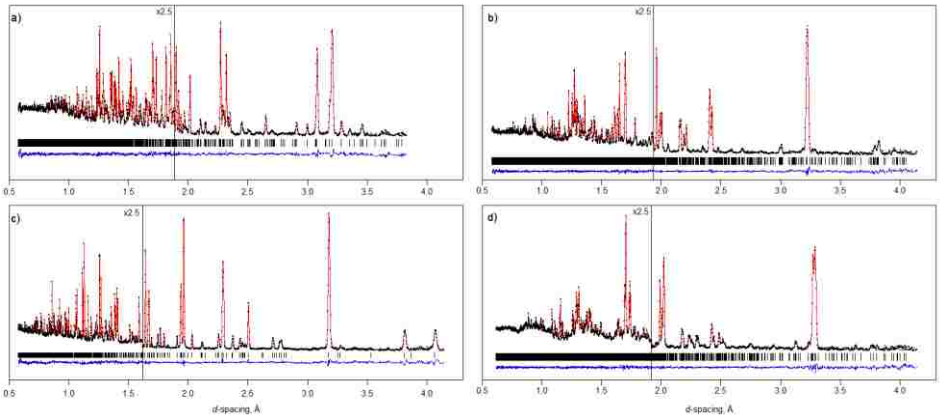

Figure 5-1: Neutron powder diffraction patterns and Rietveld fits at 400^{O}C for the (a) alpha, (b) beta, (c) LT gamma, and (d) HT gamma phases.

Phase	Alpha	Beta	LT Gamma	HT Gamma
Formula	$Bi_2Mo_3O_{12}$	$Bi_2Mo_2O_9$	Bi_2MoO_6	Bi_2MoO_6
Formula weight	897.83	753.88	609.92	609.92
Space Group	$P2_1/c$	$P2_1/n$	$Pca2_1$	$P2_1/c$
a (Å)	7.7144(1)	12.0176(2)	5.52656(5)	17.3481(3)
b (Å)	11.6251(1)	10.8625(1)	16.24558(12)	22.5253(4)
c (Å)	11.9896(1)	11.9496(2)	5.55275(5)	5.6084(1)
β (º)	114.934(1)	90.160(1)	90	90.492(1)
Volume ($Å^3$)	975.02(2)	1559.90(3)	498.538(7)	2191.52(6)
Calculated density (g/cm^3)	6.098	6.415	8.126	7.368
Impurity phase	- -	HT gamma	- -	Bi_2O_3
Impurity amount, wt%	- -	2.7	- -	3.0
Absorption coefficient	0.091	0.089	0.091	0.119
χ^2	1.787	1.473	2.720	1.411
$R_{wp,}$ %	3.28	2.67	3.58	3.06

Table 5-1: Summary of Rietveld refinement results at 400ºC under 0.01 atm O2 and 0.02 atm H2. χ2 is an average between the 300ºC and 400ºC diffraction patterns, due to certain overall parameters being fixed between these two temperatures.

While the beta and HT gamma phase materials expanded isotropically with increasing temperature, the alpha phase primarily expanded along the *b* axis, and the LT gamma phase expanded primarily along the *a* and *c* axes. The results for the lattice expansion of all four phases falls in line with previous reports in the literature[118,119]. Volumetric thermal expansion coefficients were roughly similar for all four phases, ranging from $4.1x10^{-5}$ $ºC^{-1}$ for the alpha phase to $6.3x10^{-5}$ $ºC^{-1}$ for the LT gamma phase, in the temperature range of 300-400ºC.

Two models were used for each phase: one in which the oxygen atoms had anisotropic displacements, and one in which the displacements were isotropic. Cation displacements were isotropic in both models. According to Hamilton's R-ratio test[120], the anisotropic oxygen models

led to a statistically significant improvement of the fit to the diffraction patterns. While most oxygen sites refined to 100% occupancy, certain sites refined to have vacancies in both models, so it is possible that oxygen vacancies in the materials are localized to these sites.

For the alpha phase, oxygen vacancies appear to be localized to the O4 site. This may be related to the fact that the octahedral around the molybdenum on the Mo3 site is quite distorted, making the Mo3-O4 bond distance the longest Mo-O bond in the structure: 3.007 Å at 400ºC. This may indicate a less tightly bound oxygen at this site, and parallels earlier work done by Fansuri, et al., which observed that the O4 oxygens were among the few that were more strongly affected by an exposure of their sample to an atmosphere with a pO_2 lower than that of air[118].

For the beta phase, the O16 site is most likely to be vacant. In this structure, 12 of the 18 oxygen sites have bonds to three cation sites, while 6 have bonds to only two. O16 belongs to this latter group, and within this group, has the longest Bi-O bond at 2.806 Å at 400ºC, versus 2.290-2.574 Å for the rest of the oxygen sites in this group. Similar to the case in the alpha phase, this may lead to oxygens at this site being less tightly bound than at other sites in the crystal, which could give rise to vacancies concentrating at this location. While Bi-O bond connected to this site is not the longest within the structure, all longer bonds belong to oxygen sites which have bonds to three cations and it may be the case that the greater number of bonds mitigate the weakness of the individual bonds.

For the HT gamma phase, these were the O12 and O24 sites. Both are located on the border between the Bi and Mo cation regions of the unit cell, and the longest cation-oxygen bond in the crystal is between Bi2 and O12 (3.230 Å at 400ºC), which may indicate that oxygens at this site are less tightly bound than elsewhere in the crystal. The O24 sites also align into a column that is oriented along the *c* axis and spans the entire width of the unit cell. The O12 and

O6 sites also create columns of vacancies, although vacancies on the O6 site were only observed in the anisotropic model. Columns of vacancies such as these may be indicative of oxygen transport pathways through the structure, and could be the mechanism behind this material's oxygen conductivity.

For the LT gamma phase, both models refined to have full occupancy on all oxygen sites. Evidence of oxygen conduction pathways is not clearly present, in contrast to the HT gamma phase. LT gamma has been measured to have a lower conductivity than HT gamma in the 300-400ºC region[121], so the fact that a significant number of vacancies were not observed in this temperature range is not surprising. Murugan[122] proposed that ionic conductivity in the LT gamma phase is related to the anisotropic thermal expansion of Mo-O bonds, yet we did not observe any anisotropy in the thermal expansion of apical and equatorial Mo-O bonds in the 300-400ºC region. However, when looking at displacement parameters instead of vacancies, a trend can be observed in which the oxygen sites that are sandwiched between bismuth layers, O2 and O3, have smaller displacement parameters than those surrounding the molybdenum cations. This may indicate that any conductivity present in the material at these temperatures is due to oxygens associated with molybdenum and not the oxygens in the bismuth layer.

It has been proposed that hydrocarbon oxidation, at least in the case of LT gamma, proceeds via a mechanism that involves donation of an oxygen bonded to a bismuth atom, which is then replenished by an oxygen bonded to a molybdenum atom, which is in turn replenished by oxygen from the gas phase[123]. This implies that not all regions of the crystal structure have an equal impact on catalytic activity, and therefore tuning the oxygen mobility in specific regions of the structure via vacancy concentration may be useful in improving the activity and selectivity of these catalysts. For example, Le et al. observed that, while the LT gamma phase has a higher conductivity than the beta phase, the beta material was more active

than the LT gamma material for the partial oxidation of propylene to acrolein[124], and a combination of beta and LT gamma phases was even more active. Similarly, Ono et al. observed that the beta phase was more selective than the LT gamma phase for this reaction, and a similar synergy effect was seen between the two phases[125]. An explanation for this behavior may be that, while LT gamma is a good oxygen conductor, it is the oxygens associated with the molybdenum ions that contribute the most to this conductivity, while the oxygens in the bismuth layer are less mobile. In the beta-LT gamma synergy scenario, this would fit the theory that bismuth layer oxygens in the LT gamma phase are not mobile enough to significantly contribute to hydrocarbon oxidation at the surface, but the molybdenum layers are able to replenish oxygen in surface beta phase sites more quickly than a pure beta material would be capable of.

5.3 Conclusions

Localization of oxygen vacancies were observed for three of the bismuth molybdate phases investigated: alpha, beta, and HT gamma. While oxygen vacancies were not observed in the LT gamma phase, differences in oxygen displacement parameters were measured which mesh well with previous reports on the activity and selectivity of pure LT gamma catalysts versus mixed beta/LT gamma catalysts. This highlights the importance of understanding the structural phenomena behind ionic conductivity in oxide materials, and demonstrates why total conductivity measurements alone are not enough to explain the activity and selectivity of the catalysts used for Mars van Krevelen type reactions.

6 Other Collaborative Work

In addition to the work described in the previous sections, collaboration was done as a second author on a number of other neutron diffraction projects related to SOFC materials. A synopsis of that research is detailed below.

6.1 BSCF neutron studies

$Ba_{0.5}Sr_{0.5}Co_{0.5}Fe_{0.5}O_{3-\delta}$ was examined using neutron diffraction under an atmosphere of 10% oxygen and 90% nitrogen at atmospheric pressure at temperatures ranging from 520-827ºC, and synchrotron x-ray diffraction in air at room temperature. The material was observed to have cubic Pm3̄m symmetry under all conditions, without the presence of a hexagonal phase as was previously supposed[19], or evidence of ordering for either the cation or oxygen sites. The average displacement of oxygen within the structure was found to be isotropic, in contrast to the anisotropic displacement of oxygen in the LnSCF materials. The structure was found to be significantly oxygen deficient, as well, with the non-stoichiometry parameter, δ, ranging from 0.64 at 520ºC to 0.74 at 827ºC.

Critically, the degree of oxygen non-stoichiometry was in very good agreement with previous neutron diffraction experiments performed on a similar material, $Ba_{0.5}Sr_{0.5}Co_{0.8}Fe_{0.2}O_{3-\delta}$[15], the latter being slightly more deficient in oxygen, due to substitution of iron for more cobalt causing the material as a whole to be more easily reduced. This agreement in oxygen occupancy is despite the fact that the experiments were conducted using entirely separate facilities and different methods for sample handling. In stark contrast to this consistency was the disagreement in oxygen stoichiometry in the literature among groups that measured the property using thermogravimetric analysis. While that technique is adept at

precisely measuring the change in overall oxygen stoichiometry with temperature, it requires a reference point to measure against, which can be difficult to accurately obtain. Neutron diffraction has no such limitation, as was demonstrated by this experiment.

6.2 Ruddlesden-Popper materials

This was a study of oxide materials with the Ruddlesden-Popper structure, which can be visualized as a variable number of layers of the perovskite structure sandwiched between layers of a rock salt type structure. These materials have compositions of the form $A_{n+1}B_nO3_{n+1}$, where *n* denotes the number of perovskite-type layers in between the rock salt layers. Three materials were prepared, representing the n = 1, 2, 3 structures: $LaSrCo_{0.5}Fe_{0.5}O_{4-\delta}$ (n=1), $La_{0.3}Sr_{2.7}CoFeO_{7-\delta}$ (n=2), and $LaSr_3Co_{1.5}Fe_{1.5}O_{10-\delta}$ (n=3). The unusual and inconsistent cation ratios between the samples were required in order to synthesize pure phases of each sample, as the structures have quite complex ordering. Neutron diffraction was carried out under an atmosphere of 10% oxygen and 90% nitrogen at atmospheric pressure at temperatures ranging from 492-797ºC.

In addition, pulsed oxygen isotope experiments were used to measure surface exchange rates for the samples, and the structural models derived from the neutron diffraction results were compared with this rate data. δ for the n = 1, 2, and 3 phases was obtained through the Rietveld refinement to be 0.06, 0.62, and 0.42, respectively. In general, the oxygen vacancies tended to concentrate towards the center of the perovskite layers, and were the most concentrated in the case of the n = 2 structure, with the central O3 site nearly 40% vacant, while they were more spread out in the n = 3 structure and virtually nonexistent in the n = 1 structure. In addition to the vacancy concentrations, the n = 2 phase was theorized to have the shortest hopping distance between oxygen sites, n = 1 to have the longest such distances, and n = 3 placed in between the other two structures, but closer to the n = 2 material. In line with these

results, the n = 3 material displayed oxygen exchange rates that were an order of magnitude higher than that of the n = 1 sample, and the n = 2 had even higher rates, as show in Figure 6-1.

In order to rule out differences in surface composition between the samples, high-sensitivity low energy ion scattering was performed, and the samples were nearly identical in terms of surface composition. For all three samples, the surface was almost entirely enriched with strontium, and the B site cations cobalt and iron were not present. This evidence was combined with previous results of oxygen on other perovskite oxides to put forth the hypothesis that oxygen exchange is not truly a surface reaction for these materials, but rather involves a significant portion of the bulk near the surface.

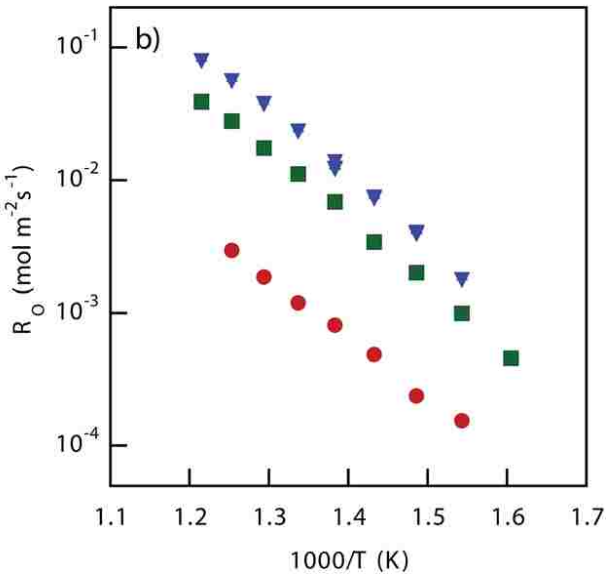

Figure 6-1 : Surface oxygen exchange rates as a function of temperature for the n = 1 (red circles), n = 2 (blue triangles), and n = 3 (green squares) Ruddlesden-Popper materials.

6.3 PBMO - layered manganite

This work utilized neutron diffraction to determine the structure of layered $PrBaMn_2O_{5+\delta}$ (PBMO). Humidified hydrogen gas of varying concentrations, from 0.08% to 50% was passed

over the sample to equilibrate it with a range of reducing gas atmospheres (pO_2 between $1\times10^{-17.9}$ and $1\times10^{-21.2}$ atm) before collecting diffraction patterns at temperatures from 419-711ºC. The oxide was determined to have tetragonal *P4/mmm* symmetry, and a perovskite type structure with alternating layers of praseodymium and barium on the A sites.

Oxygen vacancies were confined solely to the oxygen site in the praseodymium layer, O3, with O1 and O2 sites maintaining fully occupancy under all tested conditions. The O3 site was almost completely vacant under most conditions, as shown in Figure 6-2, which directly confirmed the hypothesis in the literature that the oxygen vacancies in the material layer along with the A site cations[126]. This work also proved that the material was very stable under reducing conditions: despite the wide range in oxygen partial pressures and temperatures, the material neither changed symmetry nor partitioned into separate phases.

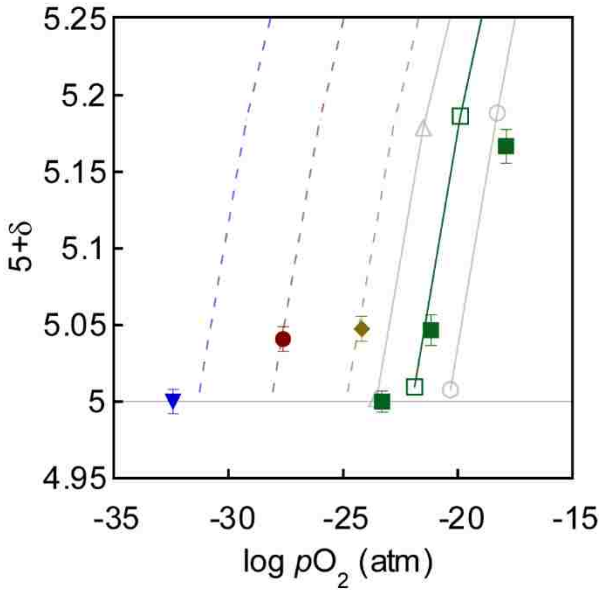

Figure 6-2 : Oxygen non-stoichiometry in PBMO as a function of the oxygen partial pressure of the gas environment. Sample temperatures were 419ºC (blue triangle), 515ºC (red circle), 613ºC (gold diamond), and 711ºC (green square). Results are compared against Sengodan[126] at 650º (open triangle), 700ºC (open square), and 750ºC (open circle).

7 Oxidative Coupling of Methane

7.1 Background on OCM

In the oxidative coupling of methane (OCM), two molecules of methane are combined into an ethylene molecule via the following reaction:

$$2CH_4 + O_2 \rightarrow C_2H_4 + 2H_2O$$

The reaction is exothermic and spontaneous, with a heat of reaction of -139 kJ per mole of methane and a Gibb's free energy of -153 kJ/mol[127], however the partial and total combustion of methane to CO, CO_2 and water is even more favorable, and indeed these are the most common side products. In order to selectively produce ethylene, the kinetics of the above reaction must be improved, and this is where the bulk of the catalytic work is focused. It has been estimated that a single pass conversion of 35-37% along with a C_{2+} selectivity of 85-88% (leading to a yield of 30-33%) is the minimum requirement for this reaction to be economically feasible[128]. Conversion is calculated according to the following formula:

$$X_{CH_4} = \frac{f_{CH_4,in} - f_{CH_4,out}}{f_{CH_4,in}}$$

Where *X* is the conversion of methane, and f is the molar flow rate of methane. The selectivity, *S*, of interest will be that of the production of C_2 hydrocarbons, and is calculated according to the following formula:

$$S_{C_2} = \frac{2f_{C_2,out}}{f_{CH_4,in} - f_{CH_4,out}}$$

Where f_{C2} is sum of the molar flowrates of ethane and ethylene.

For heterogeneous catalysis utilizing a traditional packed bed reactor with co-fed methane and oxygen, the leading catalyst for OCM is lithium-doped magnesium oxide (Li/MgO)[127]. Feeds are typically methane, oxygen, and an inert gas, with methane fed in excess, and the bed is kept at atmospheric pressure and a temperature of 600 to 800ºC. These conditions lead to selectivities in the range of 50-80% and conversions of 5-40%, culminating in yields of 15-20%. The major side products are CO and CO_2.

Currently, high selectivity towards C2+ hydrocarbons can be obtained at low (<30%) conversions, but attempts to increase conversion with current catalysts leads to a decrease in selectivity as the reaction proceeds towards combustion products such as carbon monoxide and carbon dioxide. One of the current limitations at higher temperatures may be the conversion of the desired C2 products to combustion products such as CO and CO_2. At temperatures above 740ºC over Li/MgO catalysts, 30-80% of the CO2 side products are due to complete oxidation of C2 hydrocarbons[129], placing a cap on the maximum attainable yield for these catalysts at high temperatures. At temperatures below 700ºC, however, conversion of C2 products account for less than 10% of the CO_2 produced, indicating that an increase in the performance of catalysts at these lower temperatures could be the key towards breaking the current yield barrier.

These reactions occur via a Mars van Krevelen mechanism, so oxygen conductivity may be able to influence the activity and selectivity of the catalysts used. Previous work by our lab has shown that an increase in oxygen mobility can lead to an increase in the surface oxygen exchange rate[70,116], and Taniewski et al. observed a high oxygen mobility for Li/MgO[130], one of

the current best catalysts for oxidative methane coupling[127]. We have set out to determine if these principles could be used to increase the activity of Li/MgO for the oxidative coupling of methane, as well as discover wholly novel catalysts for the process. In pursuit of this, a pair of oxygen conducting oxides, yttria stabilized zirconia (YSZ) and gadolinium doped ceria (GDC) have been selected for use as support materials for Li/MgO, in hopes that their ionic conductivity may be used to enhance the performance of Li/MgO, increasing the flux of oxygen anions to the active sites. In addition, a pair of catalysts not designed specifically for oxidative methane coupling have been chosen: the high temperature polymorph of gamma phase bismuth molybdate (HT gamma Bi_2MoO_6), and Layered $PrBaMn_2O_{5+\delta}$ (PBMO). The latter has been selected for its oxygen conductivity, and the former for its use as a partial oxidation catalyst for propylene[131], in addition to some ionic conductivity.

7.2 Results and Discussion

7.2.1 Maximum Yield Tests

In terms of yield, pure Li/MgO was the best performer, with a yield of 22% at 825ºC, followed by Li/MgO-YSZ (17.4% at 850ºC), Li/MgO-GDC (8.6% at 850ºC), Bi_2MoO_6 (6.3% at 800ºC), and PBMO (6.0% at 775ºC). This is mainly a result of the high selectivity of pure Li/MgO, which is over 80%, versus 10-40% for the other materials. Yield versus temperature for selected runs is shown in Figure 7-1, and the feed conditions for these runs are summarized in Table 7-1.

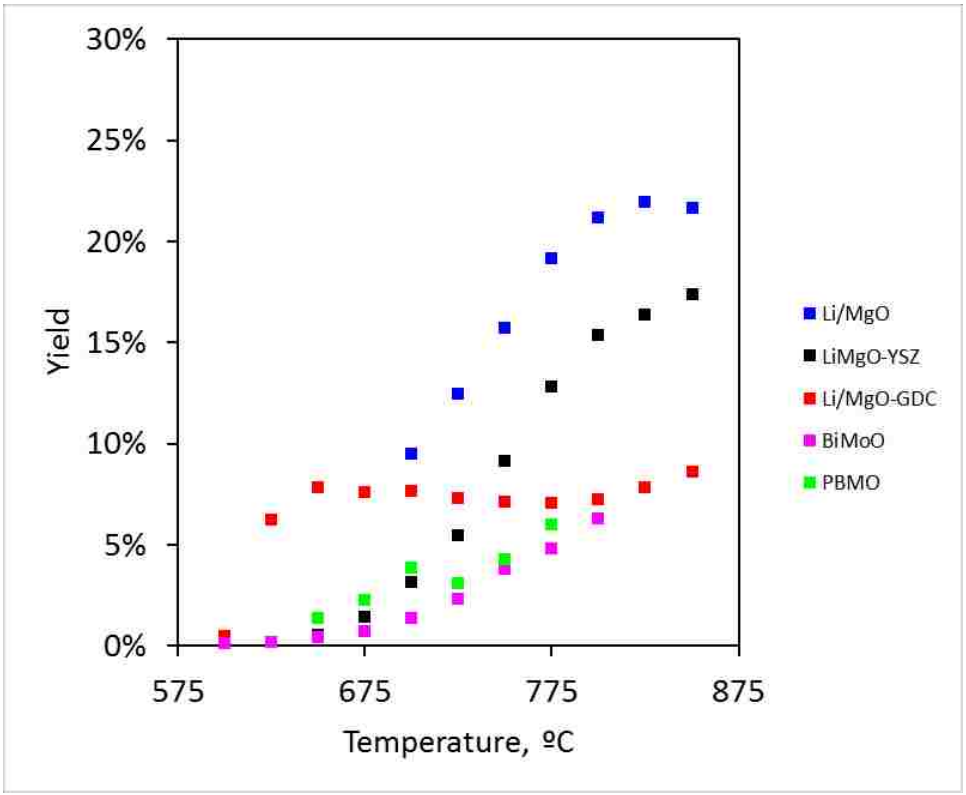

Figure 7-1 : Percent yield for each catalyst as a function of temperature.

Sample	CH4, mol%	O2, mol%	Total Flow, mL/min	Bed Volume, mL	Catalyst Mass, g
Li/MgO	40%	20%	20	1.6	1.974
Li/MgO-YSZ	4%	2%	100	0.084	0.057
Li/MgO-GDC	40%	20%	20	0.42	0.785
Bi_2MoO_6	40%	20%	5	0.85	1.525
PBMO	40%	20%	5	0.78	1.044

Table 7-1: Feed conditions and amount of catalyst loaded in the reactor for the experiments designed to maximize C2 yield.

While no material outperformed pure Li/MgO in terms of maximum yield, the GDC promoted material showed appreciable performance at low temperatures, with yields above 6% even at 625ºC. This is a promising result: Machocki[132] carried out oxidative methane coupling reactions over an Li/MgO catalyst in this temperature regime and obtained a C2+ yield of ~7% at

650ºC using a similar feed composition, versus 7.8% in this work, and estimated a ~4% yield at 625ºC, compared with the 6.2% yield obtained here for the GDC promoted catalyst. GDC is an excellent oxygen conductor[133], and it may be this property that allows it to catalyze the reaction at such low temperatures. Given that subsequent oxidation of C2 products puts a sever constraint on yield at elevated temperatures[129], operating the process at milder temperatures may be necessary to bring yields above 30%. At these lower temperatures, oxygen mobility and the rate of reduction of gaseous O_2 may be a limiting factor, similar to what is observed for solid oxide fuel cell cathodes at these temperatures[73,74].

Selectivity versus temperature is plotted in Figure 7-2. In terms of selectivity, pure Li/MgO was the clear winner, with selectivities in the range of 80-100%, dropping as conversion increased. The YSZ promoted catalyst had a slightly higher maximum selectivity than the GDC supported catalyst, peaking at 43.5% versus 33.8%, although the GDC supported catalyst maintained selectivity above 20% as the temperature dropped to 625ºC, while the selectivity of the YSZ supported catalyst steadily decreased with temperature. Once again, GDC's excellent oxygen conductivity is theorized to explain its ability to maintain its selectivity at lower temperatures than YSZ. The PBMO and Bi_2MoO6 materials possessed the lowest selectivities out of the materials tested, which follows from the fact that these materials have not been designed for oxidative methane coupling.

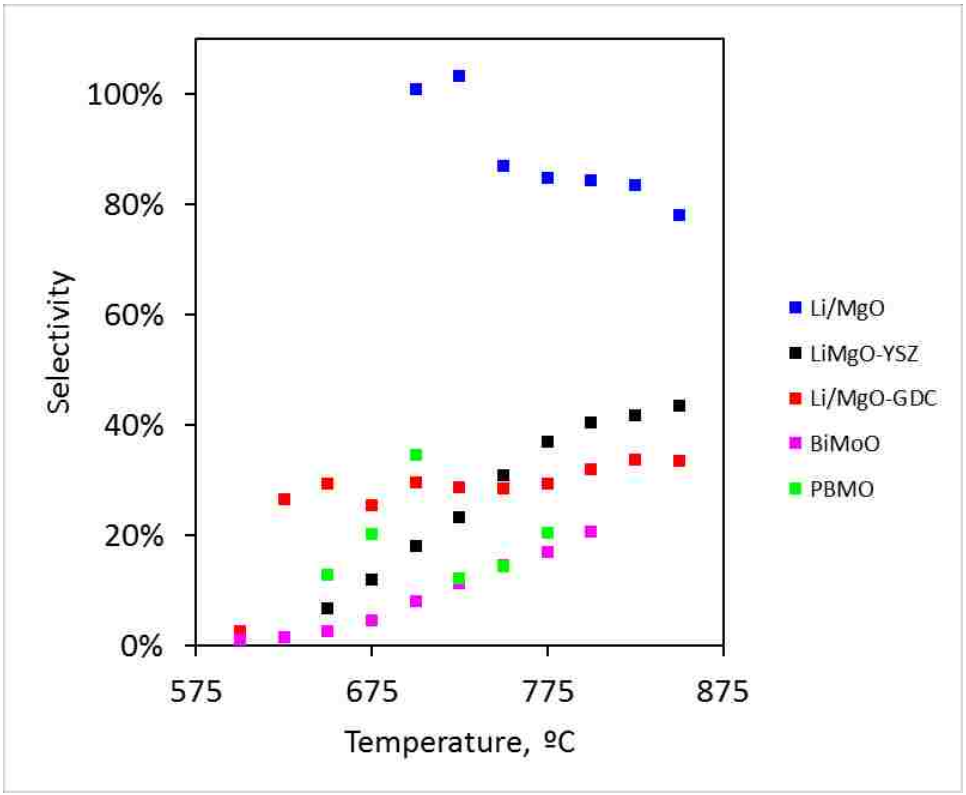

Figure 7-2 : Percent selectivity for each catalyst as a function of temperature.

7.2.2 Differential Operation

Results from operating the reactor in differential mode can be seen in Figure 7-3, where the reaction rates have been normalized by catalyst mass (catalyst + support mass in the case of YSZ and GDC supported materials), and feed conditions are summarized in **Table 7-2**. Activation energies for Li/MgO, Li/MgO-YSZ, Li/MgO-GDC, Bi_2MoO_6, and PBMO were calculated to be 122±4 kJ/mol, 152±10 kJ/mol, 224±29 kJ/mol, 212±7 kJ/mol, and 93±4 kJ/mol, respectively. In terms of activity, the Li/MgO catalyst on the YSZ support was the best performer, when normalized to catalyst + support weight. Li/MgO-YSZ performed much better than the GDC supported sample, despite the fact that the GDC support has a higher surface area, and that GDC theoretically has a higher oxygen conductivity than YSZ[133]. While this may seem in contrast

to the low temperature yield results for the YSZ and GDC promoted catalysts, the increased yield for the GDC supported material in that case was primarily due to better selectivity in the 625-675ºC range, not higher conversion. The decrease in normalized conversion could be due to other phenomena occurring at the catalyst-support interface, such as better surface wetting of the Li/MgO on YSZ versus GDC, which would lead to a greater number of active sites per unit surface area.

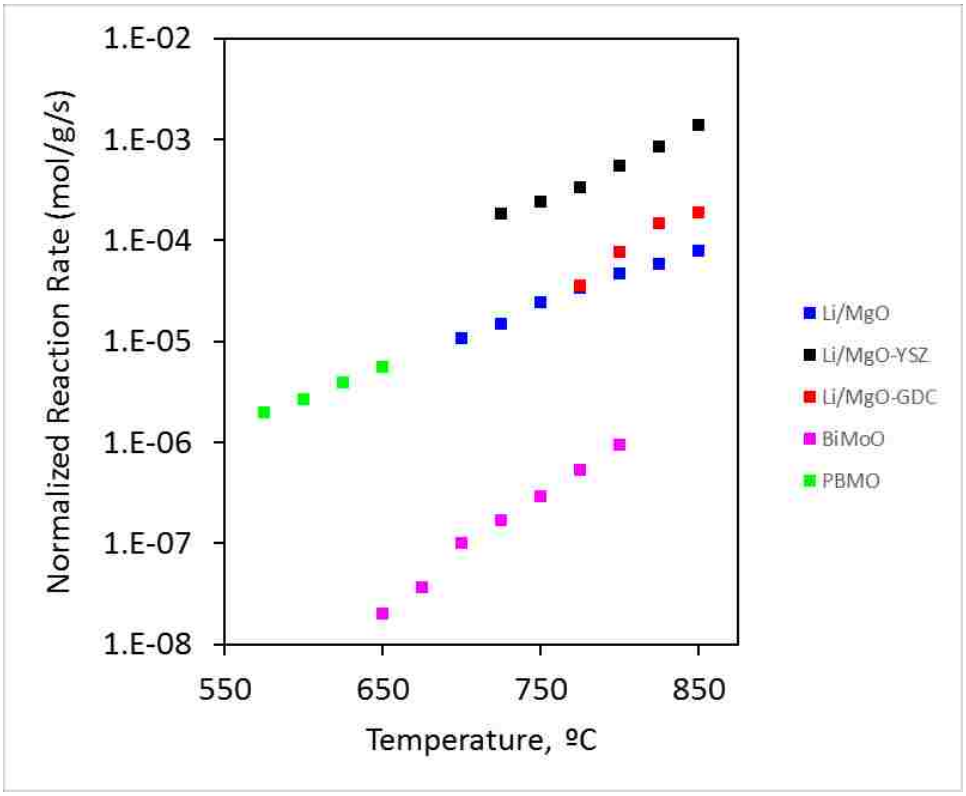

Figure 7-3 : Reaction rate based on the conversion of methane for the various catalysts, normalized by catalyst mass.

Sample	CH4, mol%	O2, mol%	Total Flow, mL/min	Bed Volume, mL	Catalyst Mass, g
Li/MgO	4%	2%	100	0.073	0.113
Li/MgO-YSZ*	20%	10%	40	0.063	$1.47x10^{-3}$
Li/MgO-GDC*	10%	5%	50	0.18	$4.95x10^{-3}$
Bi_2MoO_6	20%	10%	20	0.85	1.525
PBMO	4%	2%	100	0.78	1.044

Table 7-2: Feed conditions and amount of catalyst loaded in the reactor for the experiments run in differential mode (conversion <10%). Samples marked with an asterisk (*) were diluted with SiO2 particles, and catalyst mass given is exclusive of the diluent.

In the case of the single-phase catalyst alternatives to Li/MgO, the PBMO sample performed quite well in terms of activity, greatly outperforming the HT gamma phase bismuth molybdate material, and performing very close to Li/MgO. This appears to lend credence to the hypothesis that oxygen conductivity plays a role in the reaction. Unfortunately, PBMO begins to revert from its layered phase to a disordered phase above 800ºC[134], which prevents it from operating in the 800-850ºC region. However, it may be a promising candidate for further research into optimizing the reaction at lower temperatures, either through tuning its surface properties for higher selectivity, or as use as a support material for Li/MgO, similar to the use of YSZ and GDC in this study.

Plain MgO is a very poor catalyst for methane coupling, and it is theorized that the addition of lithium creates defects in the crystal structure, and it is these defects that are the active sites for hydrogen abstraction and the formation of the methyl radicals that couple together to form C2 hydrocarbons[135–137]. One such defect is the color center, where electrons migrate towards an oxygen vacancy in the structure, which interacts with methane as well as gas phase oxygen, and may even act as part of an oxygen pump[138]. Such vacancies are also present in many oxygen conducting oxides, such as the YSZ, GDC and PBMO of this work, and they may be a source of active sites for these materials, further increasing the performance of

these materials in addition to their ionic conductivity. These defect sites may explain the significantly higher activity of the PBMO sample versus the HT gamma phase Bi_2MoO_6 sample, since vacancies are present in nearly one in six oxygen sites in the former[134,139].

7.3 Conclusion

The results shown here implicate that oxygen conductivity may play a role in the oxidative coupling of methane, and this could be used to develop new catalysts to push the single pass yield of the process into an economically viable regime. In particular, the GDC supported samples showed a promising amount of C2 product yield at lower temperatures, and PBMO demonstrated excellent activity, despite not being designed for coupling reactions. Further research may be warranted to investigate the interaction between Li^+, MgO, and the support materials, and how their combination affects the number and properties of active sites. Tuning these relations may be key to maximize the selectivity and conversion of future materials and bring overall yield above 30 percent.

8 References

(1) Sugiura, M. Oxygen Storage Materials for Automotive Catalysts: Ceria-Zirconia Solid Solutions. *Catal. Surv. from Asia* **2003**, *7* (1), 77–87.

(2) Dove, M. T. An Introduction to the Use of Neutron Scattering Methods in Mineral Sciences. *Eur. J. Mineral.* **2002**, *14* (2), 203–224.

(3) Rietveld, H. M. A Profile Refinement Method for Nuclear and Magnetic Structures. *J. Appl. Crystallogr.* **1969**, *2* (2), 65–71.

(4) Von Dreele, R. B.; Jorgensen, J. D.; Windsor, C. G. Rietveld Refinement with Spallation Neutron Powder Diffraction Data. *J. Appl. Crystallogr.* **1982**, *15* (6), 581–589.

(5) Larson, A. C.; Von Dreele, R. B. General Structure Analysis System (GSAS). *Los Alamos Natl. Lab. Rep.* **2004**, *LAUR86-748*, 1–224.

(6) Tomkiewicz, A. C.; Tamimi, M. a.; Huq, A.; McIntosh, S. Evidence for the Low Oxygen Stoichiometry of Cubic Ba0.5Sr0.5Co0.5Fe0.5O3-δ from in-Situ Neutron Diffraction. *Solid State Ionics* **2013**, *253*, 27–31.

(7) Redfern, S. A. T.; Welch, M. D.; Henderson, C. M. B.; Knight, K. S. In Situ High- T Neutron Diffraction Studies of Non-Convergent Order/disorder in Minerals: From Simple Oxides to Complex Silicates. *Phase Transitions* **1999**, *69* (1), 17–34.

(8) MIZUSAKI, J. Nonstoichiometry, Diffusion, and Electrical Properties of Perovskite-Type Oxide Electrode Materials. *Solid State Ionics* **1992**, *52* (1-3), 79–91.

(9) Cherry, M.; Islam, M. S.; Catlow, C. R. A. Oxygen Ion Migration in Perovskite-Type Oxides. *J. Solid State Chem.* **1995**, *118* (1), 125–132.

(10) YASHIMA, M. Neutron Diffraction Study of the Perovskite-Type Lanthanum Cobaltite La0.6Sr0.4Co0.8Fe0.2O3−δ at 1260 °C and 394 °C. *Solid State Ionics* **2008**, *178* (39-40), 1939–1943.

(11) Chen, Y.-C.; Yashima, M.; Ohta, T.; Ohoyama, K.; Yamamoto, S. Crystal Structure, Oxygen Deficiency, and Oxygen Diffusion Path of Perovskite-Type Lanthanum Cobaltites La 0.4 Ba 0.6 CoO 3−δ and La 0.6 Sr 0.4 CoO 3−δ. *J. Phys. Chem. C* **2012**, *116* (8), 5246–5254.

(12) Yashima, M. In Situ Observations of Phase Transition Using High-Temperature Neutron and Synchrotron X-Ray Powder Diffractometry. *J. Am. Ceram. Soc.* **2002**, *85* (12), 2925–2930.

(13) Haag, J. M.; Barnett, S. A.; Richardson, J. W.; Poeppelmeier, K. R. Structural and Chemical Evolution of the SOFC Anode La 0.30 Sr 0.70 Fe 0.70 Cr 0.30 O 3−δ upon Reduction and Oxidation: An in Situ Neutron Diffraction Study. *Chem. Mater.* **2010**, *22* (10), 3283–3289.

(14) Shao, Z.; Haile, S. M. A High-Performance Cathode for the next Generation of Solid-Oxide Fuel Cells. *Nature* **2004**, *431* (7005), 170–173.

(15) McIntosh, S.; Vente, J. F.; Haije, W. G.; Blank, D. H. A.; Bouwmeester, H. J. M. Oxygen Stoichiometry and Chemical Expansion of Ba 0.5 Sr 0.5 Co 0.8 Fe 0.2 O 3 - δ Measured by in Situ Neutron Diffraction. *Chem. Mater.* **2006**, *18* (8), 2187–2193.

(16) McIntosh, S.; Vente, J.; Haije, W.; Blank, D. H. A.; Bouwmeester, H. J. M. Phase Stability and Oxygen Non-Stoichiometry of SrCo0.8Fe0.2O3−δ Measured by in Situ Neutron Diffraction. *Solid State Ionics* **2006**, *177* (9-10), 833–842.

(17) Mueller, D. N.; De Souza, R. A.; Yoo, H.-I.; Martin, M. Phase Stability and Oxygen Nonstoichiometry of Highly Oxygen-Deficient Perovskite-Type Oxides: A Case Study of (Ba,Sr)(Co,Fe)O 3−δ. *Chem. Mater.* **2012**, *24* (2), 269–274.

(18) Jung, J.-I.; Misture, S. T.; Edwards, D. D. Oxygen Stoichiometry, Electrical Conductivity, and Thermopower Measurements of BSCF (Ba0.5Sr0.5CoxFe1−xO3−δ, 0≤x≤0.8) in Air. *Solid State Ionics* **2010**, *181* (27-28), 1287–1293.

(19) SVARCOVA, S. Structural Instability of Cubic Perovskite BaxSr1−xCo1−yFeyO3−δ. *Solid State Ionics* **2008**, *178* (35-36), 1787–1791.

(20) Kriegel, R.; Kircheisen, R.; Töpfer, J. Oxygen Stoichiometry and Expansion Behavior of Ba0.5Sr0.5Co0.8Fe0.2O3−δ. *Solid State Ionics* **2010**, *181* (1-2), 64–70.

(21) Bucher, E.; Egger, A.; Ried, P.; Sitte, W.; Holtappels, P. Oxygen Nonstoichiometry and Exchange Kinetics of Ba0.5Sr0.5Co0.8Fe0.2O3−δ. *Solid State Ionics* **2008**, *179* (21-26), 1032–1035.

(22) Li, Y.; Maxey, E. R.; Richardson, J. W. Structural Behavior of Oxygen Permeable SrFe0.2Co0.8Ox Ceramic Membranes with and Without pO2 Gradients. *J. Am. Ceram. Soc.* **2005**, *88* (5), 1244–1252.

(23) Suescun, L.; Dabrowski, B.; Mais, J.; Remsen, S.; Richardson, J. W.; Maxey, E. R.; Jorgensen, J. D. Oxygen Ordered Phases in La X Sr 1− X MnO Y (0 ≤ X ≤ 0.2, 2.5 ≤ Y ≤ 3): An In Situ Neutron Powder Diffraction Study. *Chem. Mater.* **2008**, *20* (4), 1636–1645.

(24) Cox-Galhotra, R. A.; Huq, A.; Hodges, J. P.; Kim, J.-H.; Yu, C.; Wang, X.; Jacobson, A. J.; McIntosh, S. Visualizing Oxygen Anion Transport Pathways in NdBaCo2O5+δ by in Situ Neutron Diffraction. *J. Mater. Chem. A* **2013**, *1* (9), 3091.

(25) Cox-Galhotra, R. A.; Huq, A.; Hodges, J. P.; Yu, C.; Wang, X.; Gong, W.; Jacobson, A. J.; McIntosh, S. An in-Situ Neutron Diffraction Study of the Crystal Structure of PrBaCo2O5+δ at High Temperature and Controlled Oxygen Partial Pressure. *Solid State Ionics* **2013**, *249-250*, 34–40.

(26) Hu, Y.; Hernandez, O.; Broux, T.; Bahout, M.; Hermet, J.; Ottochian, A.; Ritter, C.; Geneste, G.; Dezanneau, G. Oxygen Diffusion Mechanism in the Mixed Ion-Electron Conductor NdBaCo2O5+x. *J. Mater. Chem.* **2012**, *22* (36), 18744.

(27) Mitchell, B. J.; Rogan, R. C.; Richardson, J. W.; Ma, B.; Balachandran, U. Stability of the Cubic Perovskite SrFe0.8Co0.2O3−δ. *Solid State Ionics* **2002**, *146* (3-4), 313–321.

(28) Speakman, S.; Richardson, J. W.; Mitchell, B. J.; Misture, S. T. In-Situ Diffraction Study of Ba2In2O5. *Solid State Ionics* **2002**, *149* (3-4), 247–259.

(29) Rolle, A.; Roussel, P.; Giridharan, N.; Suard, E.; Vannier, R. A Neutron Diffraction Study of the Oxygen Diffusion in Molybdenum Doped Ba2In2O5. *Solid State Ionics* **2008**, *179* (35-36), 1986–1995.

(30) Beznosikov, B. V.; Aleksandrov, K. S. Perovskite-like Crystals of the Ruddlesden-Popper Series. *Crystallogr. Reports* **2000**, *45* (5), 792–798.

(31) Allan, N. L.; Lawton, J. M.; Mackrodt, W. C. A Comparison of the Calculated Lattice and Defect Structures of La 2 CuO 4 , La 2 NiO 4 , Nd 2 CuO 4 , Pr 2 CuO 4 , Y 2 CuO 4 , Al 2 CuO 4 : Relationship to High- T c Superconductivity. *Philos. Mag. Part B* **1989**, *59* (2), 191–206.

(32) Allan, N. L.; Mackrodt, W. C. Oxygen Ion Migration in La 2 CuO 4. *Philos. Mag. A* **1991**, *64* (5), 1129–1132.

(33) MAZO, G. The Molecular Dynamics Study of Oxygen Mobility in La2?xSrxCuO4?? *Solid State Ionics* **2004**, *175* (1-4), 371–374.

(34) Read, M. S. D.; Islam, M. S.; King, F.; Hancock, F. E. Defect Chemistry of La 2 Ni 1 - X M X O 4 (M = Mn, Fe, Co, Cu): Relevance to Catalytic Behavior. *J. Phys. Chem. B* **1999**, *103* (9), 1558–1562.

(35) Minervini, L.; Grimes, R. W.; Kilner, J. A.; Sickafus, K. E. Oxygen Migration in La2NiO4 + δ. *J. Mater. Chem.* **2000**, *10* (10), 2349–2354.

(36) Cleave, A. R.; Kilner, J. A.; Skinner, S. J.; Murphy, S. T.; Grimes, R. W. Atomistic Computer Simulation of Oxygen Ion Conduction Mechanisms in La2NiO4. *Solid State Ionics* **2008**, *179* (21-26), 823–826.

(37) Burriel, M.; Garcia, G.; Santiso, J.; Kilner, J. A.; Chater, R. J.; Skinner, S. J. Anisotropic Oxygen Diffusion Properties in Epitaxial Thin Films of La 2 NiO 4+δ. *J. Mater. Chem.* **2008**, *18* (4), 416–422.

(38) Tonus, F.; Greaves, C.; El Shinawi, H.; Hansen, T.; Hernandez, O.; Battle, P. D.; Bahout, M. High-Temperature Redox Chemistry of La1.5+xSr0.5−xCo0.5Ni0.5O4+δ (X = 0.0, 0.2) Studied in Situ by Neutron Diffraction. *J. Mater. Chem.* **2011**, *21* (20), 7111.

(39) Skinner, S. J. Characterisation of La2NiO4+δ Using in-Situ High Temperature Neutron Powder Diffraction. *Solid State Sci.* **2003**, *5* (3), 419–426.

(40) Skinner, S. J.; Amow, G. Structural Observations on La2(Ni,Co)O4±δ Phases Determined from in Situ Neutron Powder Diffraction. *J. Solid State Chem.* **2007**, *180* (7), 1977–1983.

(41) Yashima, M.; Enoki, M.; Wakita, T.; Ali, R.; Matsushita, Y.; Izumi, F.; Ishihara, T. Structural Disorder and Diffusional Pathway of Oxide Ions in a Doped Pr2NiO4-Based Mixed Conductor. *J. Am. Chem. Soc.* **2008**, *130* (9), 2762–2763.

(42) Yashima, M.; Sirikanda, N.; Ishihara, T. Crystal Structure, Diffusion Path, and Oxygen Permeability of a Pr 2 NiO 4 -Based Mixed Conductor (Pr 0.9 La 0.1) 2 (Ni 0.74 Cu 0.21 Ga 0.05)O 4+δ. *J. Am. Chem. Soc.* **2010**, *132* (7), 2385–2392.

(43) Broux, T.; Prestipino, C.; Bahout, M.; Hernandez, O.; Swain, D.; Paofai, S.; Hansen, T. C.; Greaves, C. Unprecedented High Solubility of Oxygen Interstitial Defects in La 1.2 Sr 0.8 MnO 4+δ up to δ ∼ 0.42 Revealed by In Situ High Temperature Neutron Powder Diffraction in Flowing O 2. *Chem. Mater.* **2013**, *25* (20), 4053–4063.

(44) Bahout, M.; Tonus, F.; Prestipino, C.; Pelloquin, D.; Hansen, T.; Fonda, E.; Battle, P. D. High-Temperature Redox Chemistry of Pr0.5Sr1.5Cr0.5Mn0.5O4−δ Investigated in Situ by Neutron Diffraction and X-Ray Absorption Spectroscopy under Reducing and Oxidizing Gas Flows. *J. Mater. Chem.* **2012**, *22* (21), 10560.

(45) Tonus, F.; Bahout, M.; Battle, P. D.; Hansen, T.; Henry, P. F.; Roisnel, T. In Situ Neutron Diffraction Study of the High-Temperature Redox Chemistry of Ln3−xSr1+xCrNiO8−δ (Ln =

La, Nd) under Hydrogen. *J. Mater. Chem.* **2010**, *20* (20), 4103.

(46) Broux, T.; Bahout, M.; Hernandez, O.; Tonus, F.; Paofai, S.; Hansen, T.; Greaves, C. Reduction of Sr 2 MnO 4 Investigated by High Temperature in Situ Neutron Powder Diffraction under Hydrogen Flow. *Inorg. Chem.* **2013**, *52* (2), 1009–1017.

(47) Mogni, L. V.; Prado, F. D.; Cuello, G. J.; Caneiro, A. Study of the Crystal Chemistry of the N = 2 Ruddlesden−Popper Phases Sr 3 FeMO 6+δ (M = Fe, Co, and Ni) Using in Situ High Temperature Neutron Powder Diffraction. *Chem. Mater.* **2009**, *21* (13), 2614–2623.

(48) PRADO, F.; MOGNI, L.; CUELLO, G.; CANEIRO, A. Neutron Powder Diffraction Study at High Temperature of the Ruddlesden–Popper Phase Sr3Fe2O6+δ. *Solid State Ionics* **2007**, *178* (1-2), 77–82.

(49) Sickafus, K. E.; Wills, J. M.; Grimes, N. W. Structure of Spinel. *J. Am. Ceram. Soc.* **2004**, *82* (12), 3279–3292.

(50) Carpenter, M. A.; Salje, E. K. H. Thermodynamics of Nonconvergent Cation Ordering in Minerals; II, Spinels and the Orthopyroxene Solid Solution. *Am. Mineral.* **1994**, *79* (11-12), 1068–1083.

(51) Redfern, S.; Harrison, R. Thermodynamics and Kinetics of Cation Ordering in MgAl~ 2O~ 4 Spinel up to 1600 C from in Situ Neutron Diffraction. *Am. …* **1999**, *84*, 299–310.

(52) Pavese, A.; Artioli, G.; Hoser, A. MgAl2O4 Synthetic Spinel: Cation and Vacancy Distribution as a Function of Temperature, from in Situ Neutron Powder Diffraction. *Zeitschrift für Krist. - Cryst. Mater.* **2000**, *215* (7).

(53) O'Neill, H.; Navrotsky, A. Simple Spinels; Crystallographic Parameters, Cation Radii, Lattice Energies, and Cation Distribution. *Am. Mineral.* **1983**, *68* (1-2), 181–194.

(54) Marinoni, N.; Levy, D.; Dapiaggi, M.; Pavese, A.; Smith, R. I. In Situ High-Temperature X-Ray and Neutron Powder Diffraction Study of Cation Partitioning in Synthetic Mg(Fe0.5Al0.5)2O4 Spinel. *Phys. Chem. Miner.* **2010**, *38* (1), 11–19.

(55) Pavese, A.; Levy, D.; Hoser, A. Cation Distribution in Synthetic Zinc Ferrite (Zn0. 97Fe2. 02O4) from in Situ High-Temperature Neutron Powder Diffraction. *Am. Mineral.* **2000**, *85*, 1497–1502.

(56) Li, Y.; Maxey, E. R.; Richardson, J. W.; Ma, B. Structural and Chemical Evolution of Fe□Co□O Based Ceramics under Reduction/oxidation—an in Situ Neutron Diffraction Study. *Mater. Sci. Eng. B* **2004**, *106* (1), 6–26.

(57) Ozawa, M.; Loong, C.-K. In Situ X-Ray and Neutron Powder Diffraction Studies of Redox Behavior in CeO2-Containing Oxide Catalysts. *Catal. Today* **1999**, *50* (2), 329–342.

(58) Loong, C.-K.; Ozawa, M. The Role of Rare Earth Dopants in Nanophase Zirconia Catalysts for Automotive Emission Control. *J. Alloys Compd.* **2000**, *303-304*, 60–65.

(59) Li, Y.; Maxey, E. R.; Richardson, J. W.; Ma, B.; Lee, T. H.; Song, S.-J. Oxygen Non-Stoichiometry and Thermal?Chemical Expansion of Ce 0.8 Y 0.2 O 1.9?? Electrolytes by Neutron Diffraction. *J. Am. Ceram. Soc.* **2007**, *90* (4), 1208–1214.

(60) Loong, C. K.; Richardson, J. W.; Ozawa, M. Crystal Phases, Defects, and Dynamics of Adsorbed Hydroxyl Groups and Water in Pure and Lanthanide-Modified Zirconia: A Neutron-Scattering Study. *J. Catal.* **1995**, *157* (2), 636–644.

(61) Loong, C.-K.; Ozawa, M.; Takeuchi, K.; Ui, K.; Koura, N. Neutron Studies of Rare Earth-Modified Zirconia Catalysts and Yttrium-Doped Barium Cerate Proton-Conducting Ceramic Membranes. *J. Alloys Compd.* **2006**, *408-412*, 1065–1070.

(62) Hempelmann, R. Quasielastic Neutron Scattering Study of Proton Diffusion in SrCe0.95Yb0.05H0.02O2.985. *Solid State Ionics* **1995**, *77*, 152–156.

(63) Ozawa, M.; Suzuki, S.; Loong, C.-K.; Richardson, J. W.; Thomas, R. R. Structural Phase Transitions and Lean NO Removal Activity of Copper-Modified Alumina. *Appl. Surf. Sci.* **1997**, *121-122*, 441–444.

(64) Loong, C.-K.; Richardson, J. .; Ozawa, M. Structural Phase Transformations of Rare-Earth Modified Transition Alumina to corundum1Work Supported by US Department of Energy, BES, Contract No. W-31-109-ENG-38.1. *J. Alloys Compd.* **1997**, *250* (1-2), 356–359.

(65) Walton, R. I.; Millange, F.; Smith, R. I.; Hansen, T. C.; O'Hare, D. Real Time Observation of the Hydrothermal Crystallization of Barium Titanate Using in Situ Neutron Powder Diffraction. *J. Am. Chem. Soc.* **2001**, *123* (50), 12547–12555.

(66) Huq, A.; Richardson, J. W.; Maxey, E. R.; Chandra, D.; Chien, W.-M. Structural Studies of Deuteration and Dedeuteration of Li 3 N by Use of In Situ Neutron Diffraction. *J. Phys. Chem. C* **2007**, *111* (28), 10712–10717.

(67) Doorn, R. H. E. van; Kruidhof, H.; Nijmeijer, A.; Winnubst, L.; Burggraaf, A. J. Preparation of La0.3Sr0.7CoO3−δ Perovskite by Thermal Decomposition of Metal-EDTA Complexes. *J. Mater. Chem.* **1998**, *8* (9), 2109–2112.

(68) Toby, B. H. EXPGUI , a Graphical User Interface for GSAS. *J. Appl. Crystallogr.* **2001**, *34* (2), 210–213.

(69) Bouwmeester, H. J. M.; Song, C.; Zhu, J.; Yi, J.; van Sint Annaland, M.; Boukamp, B. A. A Novel Pulse Isotopic Exchange Technique for Rapid Determination of the Oxygen Surface Exchange Rate of Oxide Ion Conductors. *Phys. Chem. Chem. Phys.* **2009**, *11* (42), 9640–9643.

(70) Tomkiewicz, A. C.; Meloni, M.; McIntosh, S. On the Link between Bulk Structure and Surface Activity of Double Perovskite Based SOFC Cathodes. *Solid State Ionics* **2014**, *260*, 55–59.

(71) Buttrey, D. J.; Vogt, T.; Wildgruber, U.; Robinson, W. R. Structural Refinement of the High Temperature Form of Bi2MoO6. *J. Solid State Chem.* **1994**, *111* (1), 118–127.

(72) Simner, S. P.; Bonnett, J. F.; Canfield, N. L.; Meinhardt, K. D.; Shelton, J. P.; Sprenkle, V. L.; Stevenson, J. W. Development of Lanthanum Ferrite SOFC Cathodes. *J. Power Sources* **2003**, *113* (1), 1–10.

(73) Jacobson, A. J. Materials for Solid Oxide Fuel Cells. *Chem. Mater.* **2010**, *22* (3), 660–674.

(74) Adler, S. B. Factors Governing Oxygen Reduction in Solid Oxide Fuel Cell Cathodes. *Chem. Rev.* **2004**, *104* (10), 4791–4844.

(75) Kilner, J. A. Surface Exchange of Oxygen in Mixed Conducting Perovskite Oxides. *Solid State Ionics* **1996**, *86-88*, 703–709.

(76) De Souza, R. A. Oxygen Transport in La1−xSrxMn1−yCoyO3±δ Perovskites Part II. Oxygen Surface Exchange. *Solid State Ionics* **1999**, *126* (1-2), 153–161.

(77) De Souza, R. A. A Universal Empirical Expression for the Isotope Surface Exchange Coefficients (K*) of Acceptor-Doped Perovskite and Fluorite Oxides. *Phys. Chem. Chem. Phys.* **2006**, *8* (7), 890–897.

(78) Cox-Galhotra, R. A.; McIntosh, S. Unreliability of Simultaneously Determining Kchem and Dchem via Conductivity Relaxation for Surface-Modified La0.6Sr0.4Co0.2Fe0.8O3−δ. *Solid State Ionics* **2010**, *181* (31-32), 1429–1436.

(79) De Souza, R. A.; Chater, R. Oxygen Exchange and Diffusion Measurements: The Importance of Extracting the Correct Initial and Boundary Conditions. *Solid State Ionics* **2005**, *176* (23-24), 1915–1920.

(80) Baumann, F. S.; Fleig, J.; Konuma, M.; Starke, U.; Habermeier, H.-U.; Maier, J. Strong Performance Improvement of La[sub 0.6]Sr[sub 0.4]Co[sub 0.8]Fe[sub 0.2]O[sub 3−δ] SOFC Cathodes by Electrochemical Activation. *J. Electrochem. Soc.* **2005**, *152* (10), A2074.

(81) Jiang, S. Origin of the Initial Polarization Behavior of Sr-Doped LaMnO3 for O2 Reduction in Solid Oxide Fuel Cells. *Solid State Ionics* **2001**, *138* (3-4), 183–190.

(82) Wang, W.; Jiang, S. A Mechanistic Study on the Activation Process of (La, Sr)MnO3 Electrodes of Solid Oxide Fuel Cells. *Solid State Ionics* **2006**, *177* (15-16), 1361–1369.

(83) Bouwmeester, H. J. M.; Otter, M. W.; Boukamp, B. A. Oxygen Transport in La0.6Sr0.4Co1?y Fe Y O3?? *J. Solid State Electrochem.* **2004**, *8* (9), 599–605.

(84) Lane, J. Oxygen Transport in La0.6Sr0.4Co0.2Fe0.8O3−δ. *Solid State Ionics* **1999**, *121* (1-4), 201–208.

(85) Toby, B. H. Getting Started with Rietveld Refinement: An Introduction Covering Fundamental Concepts, History and the Method; Argonne National Laboratory, 2006.

(86) Sears, V. F. Neutron Scattering Lengths and Cross Sections. *Neutron News* **1992**, *3* (3), 26–37.

(87) Chantler, C. T.; Olsen, K.; Dragoset, R. A.; Chang, J.; Kishore, A. R.; Kotochigova, S. A.; Zucker, D. S. X-Ray Form Factor, Attenuation, and Scattering Tables (version 2.1) http://www.nist.gov/pml/data/ffast/index.cfm.

(88) King, G.; Woodward, P. M. Cation Ordering in Perovskites. *J. Mater. Chem.* **2010**, *20* (28), 5785.

(89) Matsumoto, Y. Oxygen Evolution on La[sub 1−x]Sr[sub x]Fe[sub 1−y]Co[sub y]O[sub 3] Series Oxides. *J. Electrochem. Soc.* **1980**, *127* (11), 2360–2364.

(90) Troyanchuk, I. O.; Karpinsky, D. V.; Efimov, V. V.; Efimova, E.; Sikolenko, V.; Yusupov, R. Crystal Structure and the Magnetic State of Pr0.5Sr0.5Co0.5Fe0.5O3. *JETP Lett.* **2008**, *87* (6), 306–310.

(91) Shannon, R. D. Revised Effective Ionic Radii and Systematic Studies of Interatomic Distances in Halides and Chalcogenides. *Acta Crystallogr. Sect. A* **1976**, *32* (5), 751–767.

(92) Armstrong, T. R. Dimensional Instability of Doped Lanthanum Chromite. *J. Electrochem. Soc.* **1996**, *143* (9), 2919.

(93) Larsen, P. H.; Hendriksen, P. V; Mogensen, M. Dimensional Stability and Defect Chemistry of Doped Lanthanum Chromites. *J. Therm. Anal.* **1997**, *49* (3), 1263–1275.

(94) McCusker, L. B.; Von Dreele, R. B.; Cox, D. E.; Louër, D.; Scardi, P. Rietveld Refinement Guidelines. *J. Appl. Crystallogr.* **1999**, *32* (1), 36–50.

(95) Saiful Islam, M. Ionic Transport in ABO3 Perovskite Oxides: A Computer Modelling Tour. *J. Mater. Chem.* **2000**, *10* (4), 1027–1038.

(96) Zawadzki, M.; Grabowska, H.; Trawczyński, J. Effect of Synthesis Method of LSCF Perovskite on Its Catalytic Properties for Phenol Methylation☆. *Solid State Ionics* **2010**, *181* (23-24), 1131–1139.

(97) Liu, Y.; Wang, F.; Chi, B.; Pu, J.; Jian, L.; Jiang, S. P. A Stability Study of Impregnated LSCF–GDC Composite Cathodes of Solid Oxide Fuel Cells. *J. Alloys Compd.* **2013**, *578*, 37–43.

(98) Dulli, H.; Dowben, P.; Liou, S.-H.; Plummer, E. Surface Segregation and Restructuring of Colossal-Magnetoresistant Manganese Perovskites La0.65Sr0.35MnO3. *Phys. Rev. B* **2000**, *62* (22), R14629–R14632.

(99) Viitanen, M. Silica Poisoning of Oxygen Membranes. *Solid State Ionics* **2002**, *150* (3-4), 223–228.

(100) Fister, T. T.; Fong, D. D.; Eastman, J. A.; Baldo, P. M.; Highland, M. J.; Fuoss, P. H.; Balasubramaniam, K. R.; Meador, J. C.; Salvador, P. A. In Situ Characterization of Strontium Surface Segregation in Epitaxial La[sub 0.7]Sr[sub 0.3]MnO[sub 3] Thin Films as a Function of Oxygen Partial Pressure. *Appl. Phys. Lett.* **2008**, *93* (15), 151904.

(101) Crumlin, E. J.; Mutoro, E.; Liu, Z.; Grass, M. E.; Biegalski, M. D.; Lee, Y.-L.; Morgan, D.; Christen, H. M.; Bluhm, H.; Shao-Horn, Y. Surface Strontium Enrichment on Highly Active Perovskites for Oxygen Electrocatalysis in Solid Oxide Fuel Cells. *Energy Environ. Sci.* **2012**, *5* (3), 6081.

(102) Druce, J.; Ishihara, T.; Kilner, J. Surface Composition of Perovskite-Type Materials Studied by Low Energy Ion Scattering (LEIS). *Solid State Ionics* **2014**, *262*, 893–896.

(103) de Ridder, M.; Vervoort, A. G. J.; van Welzenis, R. G.; Brongersma, H. H. The Limiting Factor for Oxygen Exchange at the Surface of Fuel Cell Electrolytes. *Solid State Ionics* **2003**, *156* (3-4), 255–262.

(104) Chen, D.; Wang, F.; Shi, H.; Ran, R.; Shao, Z. Systematic Evaluation of Co-Free LnBaFe2O5+δ (Ln=Lanthanides or Y) Oxides towards the Application as Cathodes for Intermediate-Temperature Solid Oxide Fuel Cells. *Electrochim. Acta* **2012**, *78*, 466–474.

(105) James, M.; Tedesco, T.; Cassidy, D. J.; Withers, R. L. Oxygen Vacancy Ordering in Strontium Doped Rare Earth Cobaltate Perovskites Ln1−xSrxCoO3−δ (Ln=La, Pr and Nd; x>0.60). *Mater. Res. Bull.* **2005**, *40* (6), 990–1000.

(106) Kharton, V. V; Kovalevsky, A. V; Patrakeev, M. V; Tsipis, E. V; Viskup, A. P.; Kolotygin, V. A.; Yaremchenko, A. A.; Shaula, A. L.; Kiselev, E. A.; Waerenborgh, J. C. Oxygen Nonstoichiometry, Mixed Conductivity, and Mössbauer Spectra of Ln 0.5 A 0.5 FeO 3−δ (Ln = La−Sm, A = Sr, Ba): Effects of Cation Size. *Chem. Mater.* **2008**, *20* (20), 6457–6467.

(107) Świerczek, K. Physico-Chemical Properties of Ln0.5A0.5Co0.5Fe0.5O3−δ (Ln: La, Sm; A: Sr, Ba) Cathode Materials and Their Performance in Electrolyte-Supported Intermediate Temperature Solid Oxide Fuel Cell. *J. Power Sources* **2011**, *196* (17), 7110–7116.

(108) Park, S.; Choi, S.; Shin, J.; Kim, G. Electrochemical Investigation of Strontium Doping

Effect on High Performance Pr1−xSrxCoO3−δ (x=0.1, 0.3, 0.5, and 0.7) Cathode for Intermediate-Temperature Solid Oxide Fuel Cells. *J. Power Sources* **2012**, *210*, 172–177.

(109) van den Bossche, M.; McIntosh, S. The Rate and Selectivity of Methane Oxidation over La0.75Sr0.25CrxMn1−xO3−δ as a Function of Lattice Oxygen Stoichiometry under Solid Oxide Fuel Cell Anode Conditions. *J. Catal.* **2008**, *255* (2), 313–323.

(110) van den Bossche, M.; McIntosh, S. Pulse Reactor Studies to Assess the Potential of La 0.75 Sr 0.25 Cr 0.5 Mn 0.4 X 0.1 O 3-δ (X = Co, Fe, Mn, Ni, V) as Direct Hydrocarbon Solid Oxide Fuel Cell Anodes. *Chem. Mater.* **2010**, *22* (21), 5856–5865.

(111) Adams, C.; Jennings, T. Mechanism Studies of the Catalytic Oxidation of Propylene. *J. Catal.* **1964**, *3* (6), 549–558.

(112) Keulks, G. The Mechanism of Propylene of Oxygen Oxidation Atom Incorporation over Bismuth into the Products Molybdate * The Catalytic Oxidation of Olefins , Using Bismuth Molybdate Catalysts , Has Received Considerable Attention during the Past Decade . Studies Invo. *J. Catal.* **1970**, *19*, 232–235.

(113) Wragg, R. D.; Ashmore, P. G.; Hockey, J. A. Selective Oxidation of Propene over Bismuth Molybdate Catalysts: The Oxidation of Propene Using 18O Labeled Oxygen and Catalyst. *J. Catal.* **1971**, *22* (1), 49–53.

(114) OTSUBO, T. Tracer Studies of Catalytic Oxidation by Bismuth Molybdate I. Hydrogen Reduction of Labeled Catalysts. *J. Catal.* **1975**, *36* (2), 240–243.

(115) KRENZKE, L. The Catalytic Oxidation of Propylene VI. Mechanistic Studies Utilizing Isotopic Tracers. *J. Catal.* **1980**, *61* (2), 316–325.

(116) Tamimi, M. a.; Tomkiewicz, A. C.; Huq, A.; McIntosh, S. On the Link between Bulk and Surface Properties of Mixed Ion Electron Conducting Materials Ln 0.5 Sr 0.5 Co 0.8 Fe 0.2 O 3−δ (Ln = La, Pr, Nd). *J. Mater. Chem. A* **2014**, *2* (44), 18838–18847.

(117) Tomkiewicz, A. C.; Tamimi, M. a.; Huq, A.; McIntosh, S. Oxygen Transport Pathways in Ruddlesden–Popper Structured Oxides Revealed via in Situ Neutron Diffraction. *J. Mater. Chem. A* **2015**, *3* (43), 21864–21874.

(118) Fansuri, H.; Zhang, D.; Elcombe, M. In-Situ Neutron Diffraction Study Of Î±-Bismuth Molybdate. In *CHEMECA*; Adelaide, Australia, 2003.

(119) Boon, L.; Baas, H. de J.; Metselaar, R. Lattice Parameters of Bismuth Molybdates Determined with a New High Temperature Diffractometer. *Powder Diffr.* **1990**, *5* (3), 152–154.

(120) Hamilton, W. C. Significance Tests on the Crystallographic R Factor. *Acta Crystallogr.* **1965**, *18* (3), 502–510.

(121) Sim, L.; Lee, C.; West, A. High Oxide Ion Conductivity in Bi2MoO6 Oxidation Catalyst. *J. Mater. Chem.* **2002**, *12* (1), 17–19.

(122) Murugan, R. Investigation on Ionic Conductivity and Raman Spectra of γ-Bi2MoO6. *Phys. B Condens. Matter* **2004**, *352* (1-4), 227–232.

(123) Dadyburjor, D. B.; Ruckenstein, E. Path of Oxygen in a Bismuth Molybdate Lattice during Selective Oxidation. *J. Phys. Chem.* **1978**, *82* (13), 1563–1575.

(124) Le, M. T.; Bac, L. H.; Van Driessche, I.; Hoste, S.; Van Well, W. J. M. The Synergy Effect

between Gamma and Beta Phase of Bismuth Molybdate Catalysts: Is There Any Relation between Conductivity and Catalytic Activity? *Catal. Today* **2008**, *131* (1-4), 566–571.

(125) Ono, T.; Utsumi, K.; Tsukamoto, S.; Tamaru, H.; Kataoka, M.; Noguchi, F. Roles of Bulk γ(L)-Bi2MoO6 and Surface β-Bi2Mo2O9 in the Selective Catalytic Oxidation of C3H6. *J. Mol. Catal. A Chem.* **2010**, *318* (1-2), 94–100.

(126) Sengodan, S.; Choi, S.; Jun, A.; Shin, T. H.; Ju, Y.-W.; Jeong, H. Y.; Shin, J.; Irvine, J. T. S.; Kim, G. Layered Oxygen-Deficient Double Perovskite as an Efficient and Stable Anode for Direct Hydrocarbon Solid Oxide Fuel Cells. *Nat. Mater.* **2015**, *14* (2), 205–209.

(127) Arndt, S.; Laugel, G.; Levchenko, S.; Horn, R.; Baerns, M.; Scheffler, M.; Schlögl, R.; Schomäcker, R. A Critical Assessment of Li/MgO-Based Catalysts for the Oxidative Coupling of Methane. *Catal. Rev.* **2011**, *53* (4), 424–514.

(128) Lu, Y.; Dixon, A. G.; Moser, W. R.; Hua Ma, Y.; Balachandran, U. Oxygen-Permeable Dense Membrane Reactor for the Oxidative Coupling of Methane. *J. Memb. Sci.* **2000**, *170* (1), 27–34.

(129) Nelson, P. F.; Cant, N. W. Oxidation of C2 Hydrocarbon Products during the Oxidative Coupling of Methane over a Lithium/magnesia Catalyst. *J. Phys. Chem.* **1990**, *94* (9), 3756–3761.

(130) Taniewski, M.; Lachowicz, A.; Lachowicz, R.; Czechowicz, D.; Skutil, K. Evidence for a High Oxygen Mobility in Li/MgO. *Catal. Letters* **1994**, *26* (3-4), 355–363.

(131) Tsunoda, T.; Hayakawa, T.; Kameyama, T.; Fukuda, K.; Takehira, K. Alkene Oxidation over the Mo-Bi Mixed oxides/Au | Yttria-Stabilized Zirconia | Ag System. *J. Chem. Soc. Faraday Trans.* **1995**, *91* (7), 1117.

(132) Machocki, A. Oxidative Coupling of Methane at Moderate (600-650??C) Temperatures. *Catal. Letters* **1994**, *26* (1-2), 85–93.

(133) Kharton, V.; Marques, F.; Atkinson, A. Transport Properties of Solid Oxide Electrolyte Ceramics: A Brief Review. *Solid State Ionics* **2004**, *174* (1-4), 135–149.

(134) Trukhanov, S. V; Lobanovski, L. S.; Bushinsky, M. V; Fedotova, V. V; Troyanchuk, I. O.; Trukhanov, a V; Ryzhov, V. a; Szymczak, H.; Szymczak, R.; Baran, M. Study of A-Site Ordered PrBaMn 2 O 6−δ Manganite Properties Depending on the Treatment Conditions. *J. Phys. Condens. Matter* **2005**, *17* (41), 6495–6506.

(135) López, T.; Gómez, R.; Ramírez-Solis, A.; Poulain, E.; Novaro, O. Li/MgO Sol-Gel Catalysts. *J. Mol. Catal.* **1994**, *88* (1), 71–84.

(136) Zavyalova, U.; Geske, M.; Horn, R.; Weinberg, G.; Frandsen, W.; Schuster, M.; Schlögl, R. Morphology and Microstructure of Li/MgO Catalysts for the Oxidative Coupling of Methane. *ChemCatChem* **2011**, *3* (6), 949–959.

(137) Richter, N. A.; Stavale, F.; Levchenko, S. V.; Nilius, N.; Freund, H. J.; Scheffler, M. Defect Complexes in Li-Doped MgO. *Phys. Rev. B - Condens. Matter Mater. Phys.* **2015**, *91* (19), 1–9.

(138) Balint, I.; Aika, K. Specific Defect Sites Creation by Doping MgO with Lithium and Titanium. *Appl. Surf. Sci.* **2001**, *173* (3-4), 296–306.

(139) Trukhanov, S. V.; Trukhanov, A. V.; Szymczak, H.; Szymczak, R.; Baran, M. Thermal

Stability of A-Site Ordered PrBaMn2O6 Manganites. *J. Phys. Chem. Solids* **2006**, *67* (4), 675–681.

9 Vita

Mazin Abdulla Tamimi

Personal

Mazin Tamimi was born in Dhahran, Saudi Arabia on March 25th, 1986 to his parents, Mary Jo and Abdulla Tamimi. His early years were spent in Saudi Arabia, but at age nine, his family moved to California's East San Francisco Bay Area, where he stayed until graduating high school. He returned to Saudi Arabia to enroll at that country's top engineering university, KFUPM. Graduating with second distinction, he began his career in the Research & Development department of the national oil company, Saudi Aramco. After only two years of employment, he was selected to take part of the organization's Advanced Degree Program, and was given the opportunity of a fully-funded scholarship for PhD studies at Lehigh University in Bethlehem, Pennsylvania.

Education & awards

Aug 2011 – Present **Lehigh University**
Bethlehem, Pennsylvania, USA

- PhD Student – Chemical Engineering

Sep 2004 – June 2009 **King Fahd University of Petroleum and Minerals**
Dhahran, Kingdom of Saudi Arabia

- Bachelor of Science – Chemical Engineering
- Second Distinction (3.56/4.0 GPA)

Oct 2008 **King Fahd University of Petroleum and Minerals Cultural Exchange Trip**

- Selected to represent the university as part of a small group of students, professors, and the Dean of Student Affairs. Was sent to France to visit various universities, research centers and museums.

Publications

"Evidence for the low oxygen stoichiometry of cubic Ba0.5Sr0.5Co0.5Fe0.5O3-δ from in-situ neutron diffraction," *Solid State Ionics*, vol. 253, pp. 27–31, Dec. 2013.

"On the link between bulk and surface properties of mixed ion electron conducting materials Ln 0.5 Sr 0.5 Co 0.8 Fe 0.2 O 3−δ (Ln = La, Pr, Nd)," *J. Mater. Chem. A*, vol. 2, no. 44, pp. 18838–18847, Sep. 2014.

"High temperature in situ neutron powder diffraction of oxides," *J. Mater. Chem. A*, vol. 2, no. 17, p. 6015, 2014.

"Is the Surface Oxygen Exchange Rate Linked to Bulk Ion Diffusivity in Mixed Conducting Ruddlesden-Popper Phases?" *Faraday Discuss.*, pp. 1–15, 2015.

"Oxygen transport pathways in Ruddlesden–Popper structured oxides revealed via in situ neutron diffraction," *J. Mater. Chem. A*, vol. 3, no. 43, pp. 21864–21874, 2015.

"Structural Analysis of $PrBaMn_2O_{5+\delta}$ under SOFC Anode Conditions by In-Situ Neutron Powder Diffraction" *Journal of Power Sources*, in press, 2016.

Industry Experience

Aug 2009 – Aug 2011 **Saudi Aramco Research & Development Center**
Process Engineer

- Responsible for data collection/analysis/modeling and daily follow-up for pilot plant runs for ultra-deep desulfurization of diesel fuel
- Designed an experiment for pilot plant testing of a catalytic process for the production of petrochemical feedstocks from petroleum cuts
- Provided engineering support for the design of future pilot plants within the center
- Acted as single point of contact between external design partners and internal teams.
- Responsible for evaluating external partner designs, with the support of internal team members

Jan 2010 – Aug 2011 **Saudi Chapter of the American Chemical Society**
Member and Registration Volunteer